



How long can you trust a Starlink TLE?

An empirical comparison of SGP4 and high-fidelity propagation against operator-updated truth across a megaconstellation

Dimitrije Jankovic

Independent researcher — astro-tools

github.com/astro-tools/paper-tle-divergence-atlas

2026-05-18

Abstract

We characterise the position-error behaviour of public Two-Line Element (TLE) propagation against operator-updated truth on the Starlink megaconstellation, sweeping 24,641 next-TLE-truth pairs across 501 satellites stratified by altitude shell (540, 550, 560 km) and platform generation (v1.0, v1.5, v2-mini) over April 2026. Each pair is propagated with both SGP4 and NASA’s General Mission Analysis Tool (GMAT) at high fidelity (EGM2008 70×70 , NRLMSISE-00 drag, Sun and Moon third-body gravity, conical-shadow SRP), and the two predictions are compared against the operator’s subsequently released ephemeris evaluated as proxy truth. Three findings emerge. First, position error follows a per-cell power law $\|\Delta\mathbf{r}(\Delta t)\| \approx A \Delta t^k$ whose fitted exponents lie in (1, 2) on every populated v2-mini cell and on the high-fidelity v1.x propagator at 540 and 560 km, while the SGP4 v1.x cells and the high-fidelity v1.x cell at 550 km are sub-linear ($k \lesssim 1$); the corpus is therefore consistent with a mixture of mean-motion bias and constant unmodelled in-track acceleration whose relative weight varies by cohort; pooled L_2 medians grow from ~ 1 km at the 6 h horizon (just beyond the operator’s ~ 4 -hour update interval) to ~ 38 km (SGP4) / ~ 76 km (high-fid) at 7 d. Second, the high-fidelity propagator initialised from a public TLE does not improve over SGP4 at any of the four staleness horizons sampled; SGP4 wins on ~ 65 –75% of pairs depending on horizon — with the v2-mini cohort at long Δt the one (cohort \times horizon) regime where high-fidelity overtakes SGP4 on a majority of pairs, visible at both populated shells. The bulk negative result decomposes into three mechanisms — at-epoch operator-OD residual dominance, SGP4-vs-SGP4 truth-construction kernel alignment, and preferential spacecraft-property bias amplification on the high-fidelity arm. Third, an exploratory regression of the per-satellite SGP4 staleness coefficient against F10.7 returns a positive slope at one of three altitude shells (560 km) that clears conventional significance, with the other two shells slope-ambiguous on the present 30-day, moderate-activity, ~ 17 sfu window; we read the H3 evidence as direction-consistent with the LEO density-gradient expectation but *not* a calibrated F10.7-modulation measurement on this corpus. Practitioners should regard public Starlink TLEs as adequate inside the operator’s update cadence, treat the per-cell power-law fits as cohort-resolved staleness budgets, and avoid investing in high-fidelity propagation from public-TLE inputs unless improved initial states are also available. All code, the locked corpus, the resumable sweep manifest, and the rendered figures are released together under the MIT license.

1 Introduction

The orbital population in low Earth orbit (LEO) has shifted from a sparse collection of single-platform missions to large operator-fielded megaconstellations within a single decade, with SpaceX’s Starlink alone accounting for the majority of active payloads below 600 km [McDowell, 2020]. The public Two-Line Element (TLE) data product, derived by the United States Space Force from radar and optical observations and propagated with the analytic SGP4 model, remains the de facto state input for academic conjunction-analysis pipelines, commercial space-situational-awareness toolchains, and independent observers — none of whom has access to operator-internal orbit-determination state or onboard GNSS solutions. The operational character of TLE delivery has, however, evolved with the constellation era: Starlink TLEs publish at roughly

six updates per satellite per day, an order of magnitude faster than the once-per-day cadence assumed by the prior TLE-accuracy literature [Vallado et al., 2006, Vallado and Cefola, 2012]. The operationally relevant staleness question for a present-day TLE consumer is therefore measured in hours, not weeks — the boundary between fresh and stale lies within a single operator-update interval, and an error budget framed against propagation horizons of seven days under-represents the regime in which most downstream tools actually operate.

The next-TLE-as-truth methodology developed by Vallado et al. [2006], Vallado and Cefola [2012], and Vallado and Crawford [2008] established the analytic apparatus for measuring SGP4 accuracy from the operator’s own subsequently released ephemeris. Those studies were necessarily small in scale: a handful of well-tracked individual platforms, observed at the update cadences typical of their era. The constellation-scale, multi-generation, public-data regime that emerged with Starlink opens three questions that the original analysis was not positioned to address. First, how the SGP4 propagation error scales with time since epoch across orbital regime and platform generation in the consumer-relevant horizon range. Second, whether the high-fidelity force models routinely available in modern open-source mission-analysis tools materially improve accuracy when initialised from a TLE whose own orbit-determination residual is already non-zero at epoch. Third, whether short-window solar-flux modulation of thermospheric density is detectable in the empirical error-growth coefficients of a confined operational fleet.

We address the three questions by sweeping 24,641 starting-TLE / next-TLE pairs across 501 Starlink satellites, stratified by altitude shell (540, 550, 560 km) and platform generation (v1.0, v1.5, v2-mini) over the one-month window of April 2026. Each pair is propagated both with SGP4 from the starting TLE and with a high-fidelity propagation in NASA’s General Mission Analysis Tool (GMAT), and the two predictions are compared against the operator’s next-TLE position evaluated as proxy truth. We fit a per-cell power-law staleness curve $\|\Delta\mathbf{r}(\Delta t)\| \approx A \Delta t^k$ with satellite-level bootstrap uncertainties (Hypothesis H1, Figures 2 and 3; parametrised in Figure 4 and Table 5), test pair-by-pair whether the high-fidelity propagator beats SGP4 (Hypothesis H2, Figure 5), and regress the per-satellite coefficient A against the daily observed F10.7 flux in the most-drag-sensitive shell (Hypothesis H3, Figure 7). The data-preparation pipeline, the locked corpus, the resumable manifest of every sweep run, and the manuscript \LaTeX source are released together as an open-source artefact under the MIT licence; the sweep output bundle is deposited on Zenodo and fetched automatically by the manuscript build, so a clean re-render does not require local installation of GMAT. Section 2 reviews the methodological lineage; Section 3 specifies the corpus, force model, and error metrics; the results, their interpretation, and the practical consequences for downstream TLE consumers follow in Sections 4–6.

2 Background and related work

SGP4 is the analytic averaged-element propagator paired with the TLE format and standardised through the open-source reference implementation distributed with Vallado et al. [2006]. It expresses the mean motion and Brouwer mean elements at epoch, applies analytic secular corrections for J_2 , J_3 , and J_4 together with long- and short-period perturbation series, and absorbs atmospheric drag into a single fitted scalar B^* representing the mean ballistic coefficient encountered during the orbit-determination window. Hoots et al. [2004] trace the development of the model family inside the U.S. space-surveillance system, and Vallado [2013, §11.6] gives the textbook formulation. Two operationally relevant properties recur throughout the present analysis: the state delivered by SGP4 lives in the True Equator, Mean Equinox (TEME) frame — not in a standard inertial frame — and the fitted B^* encodes the thermospheric density encountered *during* the orbit-determination window rather than during the forward propagation that consumers subsequently perform.

The use of an operator’s subsequently released TLE as a truth proxy for prediction accuracy was introduced by Vallado et al. [2006] alongside the open-source SGP4 reference implementation, and was developed methodologically by Vallado and Cefola [2012] and applied to single-satellite orbit determination by Vallado and Crawford [2008]. In that approach the position obtained by propagating TLE_i forward to a later epoch t_j is compared against $\text{SGP4}(\text{TLE}_j, \Delta t = 0)$, i.e. the operator’s subsequently released ephemeris evaluated at its own epoch. The proxy is not a ground-truth measurement but a self-consistency check against the operator’s own orbit determination, and it inherits whatever observation-fit residual is present in the next

TLE. Its principal merit for an open-data study is that it requires no privileged access to tracking observations or operator-internal state vectors, which permits constellation-scale application from a single archived TLE history. The operator’s orbit determination is itself smoothed over a fit window of order 1–2 days, so the resulting B^* and mean motion at epoch are averaged quantities rather than instantaneous ones — relevant later for the F10.7-modulation interpretation in Section 4.

2.1 Interpretational limits of next-TLE-as-truth

The next-TLE proxy is not a ground-truth measurement, and treating it as one would overclaim the precision of the comparison. A position error measured against SGP4($\text{TLE}_j, \Delta t = 0$) decomposes into three contributions:

$$\underbrace{\Delta \mathbf{r}_{\text{obs}}(t_j)}_{\text{what we measure}} = \underbrace{\Phi(t_j, t_i) \Delta \mathbf{r}_{\text{OD}}(t_i)}_{\text{epoch-}t_i \text{ OD residual, propagated}} + \underbrace{\Delta \mathbf{r}_{\text{prop}}(t_i \rightarrow t_j)}_{\text{propagator error}} - \underbrace{\Delta \mathbf{r}_{\text{OD}}(t_j)}_{\text{epoch-}t_j \text{ OD residual}}, \quad (1)$$

where $\Delta \mathbf{r}_{\text{OD}}$ denotes the operator’s observation-fit residual at the indicated epoch and Φ is the state-transition matrix of the chosen propagator over $(t_i, t_j]$. Throughout this paper, every reported error norm $\|\Delta \mathbf{r}_{\text{SGP4}}\|$ or $\|\Delta \mathbf{r}_{\text{hifi}}\|$ is the left-hand side of Eq. (1); the propagator term in the middle cannot be cleanly isolated from observation residuals at either epoch using public TLEs alone.

The practical consequence is a regime split. At long staleness ($\Delta t = 7$ days, where Section 4 reports median observed errors of 40–80 km) the OD-residual terms in Eq. (1) are at the percent level relative to the observed total (we quantify the floor at order 1 km empirically below), and the propagator term dominates whether evaluated with SGP4 or with a high-fidelity force model. At the operationally relevant 6 h horizon, where Section 4 reports a pooled median observed error of ~ 1 km, the OD-residual floor is the same order as the signal itself.

No operator publishes an internal OD-residual figure for Starlink. The three public quantifications closest to the question bracket it from different sides, none of them an exact match. Lang and Jiang [2025] apply a third-party unscented batch filter to maneuvering Starlinks and recover 24-hour position predictions with RMS error below 3 km. The commercial radar tracking service described in the eoPortal [2022] survey reports state estimates better than 1 km at time of estimation for $\sim 95\%$ of LEO objects (and better than 200 m for $\sim 50\%$), without distinguishing Starlink from the broader population. SpaceX’s own narrative submission to the FCC on positioning, navigation, and timing [Space Exploration Holdings, LLC, 2025] discusses terminal-segment metric-precision positioning but does not publish a satellite OD residual. None of these directly answers Eq. (1): Lang and Jiang [2025] and eoPortal [2022] characterise third-party OD pipelines that observe the constellation *less* precisely than the operator does — SpaceX has onboard GNSS on every satellite — so the operator-internal residual at t_j is plausibly tighter than the ~ 1 km outer bound those third-party pipelines place on it; and the FCC submission targets user-equipment positioning, not space-segment OD. We therefore measure the floor directly with the diagnostic below.

We quantify the floor empirically by repeatedly propagating TLE_{j-N} to t_j with the same GMAT high-fidelity configuration the main sweep uses (Section 3.6) and comparing to SGP4($\text{TLE}_j, \Delta t = 0$) for $N \in \{1, 2, 3, 6\}$. To capture inter-cohort variation rather than over-generalising from a single representative, the diagnostic runs the densest-sampled corpus satellite in each of the eight populated (altitude shell \times generation) cells of Table 2 — 122–131 TLEs per sat, 3,121 arcs in total after the 100 m SMA-jump maneuver filter of Section 3.3. Per-cohort medians at the shortest arc ($N = 1, \Delta t \approx 4\text{--}5$ h) are listed in Table 1. Two features of the table carry the interpretation. First, every populated cohort sits in 0.81–1.37 km at the 5 h scale; the floor is, to within a factor of two, *cohort-independent* — v2-mini is not measurably worse than v1.5, and altitude separates the cohorts only weakly. Second, the pooled $N = 1$ median of 1.11 km (IQR 0.23–2.89 km) already exceeds the SGP4 pooled median at $\Delta t = 6$ h reported in Section 4, which is the empirical statement of floor limitation: even with a strictly better propagator *and* a strictly fresher starting TLE, the residual against the proxy truth cannot drop below $\mathcal{O}(1)$ km regardless of cohort, because that floor is built into the two TLE-derived states it is constructed from. The 6 h headline reported below should be read accordingly — as a measurement constrained by the precision of public TLE delivery, not by propagator skill, and constrained *uniformly* across the corpus.

The constellation-era context is set by two recent results. McDowell [2020] documents the shift in the LEO satellite population during the first phase of Starlink deployment and quantifies the resulting change

Table 1: Empirical truth-floor diagnostic, per (altitude shell \times generation) cohort. Each row is the densest-sampled corpus satellite in that cell, swept across $N \in \{1, 2, 3, 6\}$ TLE offsets back from TLE $_j$; the reported $|\Delta\mathbf{r}|$ is measured against SGP4(TLE $_j$, $\Delta t = 0$) at t_j . Only the shortest-arc median is tabulated for compactness; larger N trends are in the diagnostic JSON. All arcs survive the 100 m SMA-jump maneuver filter. The 540 km \times v2-mini cell is empty in the corpus (Table 2).

Shell (km)	Gen	NORAD	TLEs	arcs ($N=1$)	Δt (h)	median $ \Delta\mathbf{r} $ (km)	IQR (km)
540	v1.0	48555	122	64	4.4	1.02	0.01–2.98
540	v1.5	49766	125	123	4.8	1.17	0.23–4.10
540	v2-mini	—	—	—	—	—	—
550	v1.0	48306	106	60	4.0	0.94	0.12–4.01
550	v1.5	53675	131	112	4.8	1.19	0.53–3.05
550	v2-mini	65384	127	123	4.8	1.11	0.01–2.75
560	v1.0	48881	124	123	4.8	1.31	0.50–2.39
560	v1.5	56495	129	128	4.8	0.81	0.23–1.90
560	v2-mini	63926	125	111	4.8	1.37	0.01–3.64
<i>Pooled across cohorts</i>				844	—	1.11	0.23–2.89

in object density at the operational shells. Baruah et al. [2024] models the loss of 38 Starlink v1.5 satellites during the February 2022 moderate geomagnetic storm using a shark-fin ram area of 4.48 m² at $C_D = 1$, and provides the per-generation drag cross-section anchor reused in Section 3.4. Peer-reviewed quantitative work on public-TLE accuracy at constellation scale in the megaconstellation era remains sparse; the present paper is intended in part to address that gap.

Complementary recent work has focused on *extending* SGP4 to close the gap with numerical propagators rather than measuring the gap. SGP4-XP [Payne et al., 2022] extends the standard SGP4 analytic perturbation series with refined lunisolar gravity, generalised resonance handling, solar radiation pressure for high area-to-mass-ratio objects, and improved atmospheric density modelling near Earth, while preserving the SGP4 evaluation budget and the TLE input format. The differentiable-SGP4 line of work [Acciarini et al., 2025] reimplements the SGP4 analytic kernel in a differentiable framework so the propagator can be fine-tuned with gradient-based methods against observed ephemerides, and composed with neural-network residual correctors. Our contribution is orthogonal: we empirically characterise the baseline SGP4 versus high-fidelity behaviour on an operator megaconstellation using only the public TLE format, and the per-cell (A, k) power-law table summarised in Section 4 is in a form usable as a benchmark target by enhanced-propagator work of either flavour.

Operational LEO satellites maneuver, and a TLE pair whose interval encloses a station-keeping burn violates the no-maneuver assumption behind the next-TLE-as-truth comparison. Lemmens and Krag [2014] introduced the standard public-domain technique for detecting maneuvers from TLE histories: a jump in the semi-major axis derived from the TLE mean motion, exceeding a per-platform threshold tuned against the underlying orbit-determination noise floor, flags a station-keeping event. Starlink’s krypton Hall-effect station-keeping cadence consists of continuous low-thrust burns rather than the impulsive chemical maneuvers studied at the time of Lemmens and Krag [2014], so the threshold used here is calibrated empirically against the bimodal $|\Delta a|$ distribution of the full per-satellite TLE history within the analysis window (Appendix A, Figure 8).

3 Data and methods

3.1 TLE corpus and observation window

We work from a single one-month observation window, 2026-04-01 to 2026-05-01 UTC, pinned in the repository as `src/static/window.json` so that re-runs and Zenodo deposits remain bit-identical. The Two-Line Element archive for that window was retrieved once from the Space-Track `gp_history` endpoint restricted to `OBJECT_NAME ~ STARLINK`, yielding 1,054,157 elements across 10,363 distinct catalog identifiers. The raw

cache is held outside the public repository to honour Space-Track’s redistribution terms; the downstream sample on which all reported results depend is committed as `src/static/tles_cache.parquet`.

Starlink’s operational update cadence of approximately six TLEs per satellite per day — compared with the once-per-day cadence assumed in the prior-era literature [Vallado et al., 2006, Vallado and Cefola, 2012] — has two practical consequences for corpus construction. First, the typical interval between consecutive TLEs for a single satellite is of order four hours, well short of the propagation horizons of interest; constructing pairs from strict consecutive elements would cluster the entire corpus at a single staleness point. Second, the dense per-satellite history makes maneuver detection at the semi-major-axis-jump level statistically robust, since on the order of 180 TLE epochs per satellite are available within the observation window. We exploit both features by sampling starting TLEs at one per satellite-day and searching for matching end TLEs at four discrete target offsets (Section 3.3), and by running maneuver detection over the complete per-satellite history rather than only on the pair endpoints. The geometric distribution of the sampled satellites in (a, e, i) space is shown in Figure 1.

3.2 Stratified satellite sampling

Stratified sampling is performed over three altitude shells corresponding to the active Starlink operational layers within the analysis window. The shells are defined by the geocentric altitude derived from each satellite’s history-median TLE-mean-motion semi-major axis: 533–547 km (the 540 shell), 547–557 km (the 550 shell), and 557–573 km (the 560 shell). Use of the per-satellite median, rather than a single-TLE altitude, avoids misclassifying satellites whose TLE history straddles an orbit-raising or station-keeping maneuver. From the satellites whose median altitude falls inside one of the three shells we draw 167 without replacement per shell, using a fixed pseudo-random seed (20260401) and yielding 501 sampled satellites. The (shell \times generation) population of the resulting sample is set by Starlink’s deployment history rather than by the sampling procedure: the 540 shell carries no v2-mini coverage in the analysis window, while the 550 and 560 shells contain a mix of generations (Figure 1, Table 2).

From each sampled satellite’s per-window TLE history we draw one starting TLE per satellite-day — specifically, the earliest available epoch at or after 00:00 UTC of each day in the analysis window. The one-per-day subsampling has two motivations. First, Starlink’s $\sim 6\times$ /day publication cadence would otherwise multiply-count nearly-identical operator OD epochs into a corpus of strongly within-sat correlated pairs, inflating effective sample size without adding statistical leverage. Second, choosing the earliest daily epoch deterministically (rather than a random TLE within each day) makes the corpus bit-reproducible without recourse to an additional seed beyond 20260401 above. The starting-TLE count of 14,917 across the 501 sampled sats reflects $\lesssim 30$ days of starting epochs per sat, less the small number of sat-days with no TLE on record ($\lesssim 1\%$ of expected sat-day cells).

3.3 Pair construction and maneuver filter

For each sampled starting TLE we search the satellite’s own history for the element whose epoch is nearest to $t_i + \Delta t$ within a ± 2 h tolerance, for each target offset $\Delta t \in \{6, 24, 72, 168\}$ h. We adopt 6 h as the shortest target offset because it lies just beyond Starlink’s typical ~ 4 h operator-update interval — the boundary between fresh and stale from the consumer’s perspective and the regime in which downstream consumer tools most often operate. The remaining offsets at 1, 3, and 7 days span the short-, medium-, and long-staleness ranges over which the power-law staleness curve assumed in Hypothesis H1 is statistically meaningful.

The ± 2 h matching tolerance can in principle bias the corpus against periods of poor operator tracking: a starting epoch straddled by a multi-hour gap in the per-sat history would fail to produce a pair at one or more Δt targets. Across the 501-sat corpus and its $\sim 56,000$ in-window TLEs the median inter-TLE interval is 4.8 h (90th percentile 15.9 h, 99th percentile 23.9 h, single maximum 108 h); 17.6% of consecutive intervals exceed 12 h, and the median satellite has a longest within-window gap of 25.5 h, rising to 41.7 h at the 95th percentile across sats. Empirically, 51% of (starting TLE $\times \Delta t$) attempts produce a matched pair within the ± 2 h tolerance and the rest do not (60.6% unmatched at $\Delta t = 6$ h, 32.1% at 1 d, 43.9% at 3 d, 59.3% at 7 d). The high unmatched fractions are dominated by the Poisson-window character of the matching — the 4 h target window is the same order as the typical inter-TLE spacing, so a randomly-placed

target window has only an $\sim 50\%$ chance of containing any TLE even in dense tracking conditions — rather than by tracking-gap selection. Of the 30,451 matched candidates, 24,641 (81%) survive the Section 3.3 maneuver filter to enter the locked corpus. The bias toward well-tracked sat-days is quantitatively bounded: the 95th-percentile worst per-sat gap of ~ 42 h is well inside the longest Δt target (168 h), so no satellite is systematically excluded; the conclusions of Section 4 characterise propagator behaviour during sat-days the operator successfully covered. Both distributions are visualised in Figure 10 (Appendix E).

A pair $(\text{TLE}_i, \text{TLE}_j)$ is retained only if no maneuver was detected anywhere inside the half-open interval $(t_i, t_j]$. The maneuver detector applies the semi-major-axis-jump technique of Lemmens and Krag [2014] to every consecutive TLE pair in the satellite’s full history: the consecutive change in the mean-motion-derived semi-major axis $|\Delta a|$ is compared against a 100 m threshold, and any TLE whose preceding step exceeds the threshold is flagged as the timestamp of a station-keeping event. The threshold is calibrated empirically against the $|\Delta a|$ histogram of the entire Starlink TLE archive within the window (Appendix A, Figure 8). The per-step formulation is the dominant detection signature for Starlink’s krypton Hall-effect thrusters because the station-keeping cadence is burst-scheduled with multi-hour gaps rather than continuous; for a hypothetical steady-state low-thrust drift mode whose per-step $|\Delta a|$ never crosses 100 m but which integrates to a meaningful displacement over several days, the filter is in principle blind, a known limitation of the SMA-jump approach formalised by Lemmens and Krag [2014, §3.2]. A threshold sensitivity at $\{50, 100, 200\}$ m on the same locked corpus quantifies the effect of that limitation on the headline medians and is reported in Appendix D. After applying the filter, the locked sweep corpus contains 24,641 surviving pairs; the decomposition by altitude shell and Starlink generation is given in Table 2.

Table 2: Composition of the locked sweep corpus by altitude shell and Starlink generation. Counts give the number of surviving $(\text{TLE}_i, \text{TLE}_j)$ pairs after the maneuver filter; column and row totals aggregate across the four Δt buckets.

Shell (km)	v1.0	v1.5	v2-mini	Total
540	52	7,427	—	7,479
550	37	2,586	6,908	9,531
560	65	4,629	2,937	7,631
Total	154	14,642	9,845	24,641

3.4 Spacecraft properties

Per-satellite dry mass is taken from McDowell’s General Catalog of Artificial Space Objects [McDowell, 2020], which resolves at the launch-batch level across the Starlink generations in our corpus. Generation (v1.0 / v1.5 / v2-mini) is classified from the same catalog’s `PLName` field.

3.5 Attitude regime and drag-area choice

A Starlink satellite at its operational altitude maintains a “shark-fin” attitude — solar arrays held edge-on to the ram direction and phased-array antennas pointing toward nadir — as the station-keeping configuration. A high-drag “open-book” attitude is engaged only during autonomous collision-avoidance maneuvers and controlled de-orbit. SpaceX’s most recent semi-annual constellation status report [Space Exploration Holdings, LLC, 2024] attributes an average of 14 thruster firings per satellite over the six-month window 1 December 2023 through 31 May 2024 to autonomous collision avoidance, against continuous on-station thrust for station-keeping [Lang and Jiang, 2025]; the open-book residence fraction is therefore small, event-driven, and concentrated on intervals that the maneuver filter (Section 3.3, Appendix A) removes from the corpus before any pair reaches the sweep.

We adopt the shark-fin value as the duty-cycle-representative drag area: 2.0 m^2 at $C_D = 2.2$ for v1.0 and v1.5 (matching Baruah’s 4.48 m^2 at $C_D = 1$ to within the rounding in Table 3), and 4.5 m^2 at $C_D = 2.2$ for v2-mini (scaled from the v1.x shark-fin value by a factor of 2.25 to reflect the larger v2-mini bus). The full attitude swing from shark-fin to open-book is a factor of $4.48\times$ change in $C_D \cdot A$, which is well outside the $\pm 20\%$ uncertainty range explored in Appendix C; the sensitivity test is calibrated to bound the bus-scaling

Table 3: Per-attitude effective drag areas at the two C_D conventions, with the per-generation values used in the main sweep in the bottom block. Baruah ram areas are quoted at $C_D = 1$; the sweep uses the free-molecular-flow $C_D = 2.2$ convention, so the effective area at $C_D = 2.2$ is the Baruah value divided by 2.2. The v2-mini row has no published ballistic-coefficient analysis and is scaled from the v1.x shark-fin value by the bus-size ratio reported in Krebs [2024].

Attitude / configuration	$C_D=1$ area (m ²)	$C_D=2.2$ area (m ²)	Ratio vs. open-book
Open-book (CAM / de-orbit) [Baruah et al., 2024]	1.00	0.45	1.00×
Shark-fin (operational) [Baruah et al., 2024]	4.48	2.04	4.48×
v1.0 / v1.5 (sweep, shark-fin)	4.4	2.0	4.40×
v2-mini (sweep, shark-fin × bus-size)	9.9	4.5	9.90×

and mass-estimate uncertainty within the operational attitude, not to span the attitude swing itself (which is excluded from the corpus by construction).

3.6 Force model and integrator

The high-fidelity arm of the comparison propagates each starting state forward to t_j using NASA’s General Mission Analysis Tool (GMAT) release R2026a, configured as in Table 4. The static configuration is identical for every run; the per-pair quantities (epoch, Cartesian state in MJ2000Eq, dry mass, drag and solar-radiation-pressure coefficients and effective areas, and the integration duration) are injected into the mission script through GMAT’s field-override interface ahead of each call to the mission sequence.

Table 4: High-fidelity force-model and integrator configuration applied to every sweep run. The values listed are identical across all 24,641 propagations; per-pair quantities (initial state, epoch, dry mass, drag and SRP coefficients and effective areas, propagation duration) are supplied through GMAT’s field-override interface and are not shown here.

Component	Setting	Reference
Central body	Earth	—
Gravity field	EGM2008, degree 70, order 70	Pavlis et al. [2012]
Third bodies	Sun, Moon (point masses)	—
Solar radiation pressure	Enabled, conical Earth shadow	GMAT R2026a default
Atmospheric drag	NRLMSISE-00	Picone et al. [2002]
Integrator	Runge–Kutta 8(9)	Verner [1978]
Accuracy tolerance	10^{-12} km	—
Initial step	60 s	—
Minimum / maximum step	10^{-3} s / 600 s	—
Error-control mode	RSS step	—

EGM2008 is loaded at degree and order 70 from a project-installed coefficient file produced by parsing the NGA flat-text `EGM2008_to2190_TideFree` distribution into the GMAT `.cof` format; the truncation error at degree 70 relative to the full 2160×2160 expansion is small enough at LEO altitudes [Pavlis et al., 2012] that it sits well below the integrated drag and operator-OD-residual contributions to the kilometre-scale position errors characterised by this analysis, and is not load-bearing for any of the comparisons that follow. Atmospheric drag uses GMAT’s NRLMSISE-00 implementation [Picone et al., 2002], the SSA community standard for thermospheric density at LEO altitudes; the integrator reads CSSI-format F10.7 and Ap inputs from the project-local space-weather file described in Section 3.9. The F10.7 and Ap values reported per output row in Section 3.8 are an independent analysis annotation joined onto each row at post-processing time and play no role in the integration. The 8(9)-order Runge–Kutta scheme with embedded error estimator

[Verner, 1978] held the configured tolerance across the longest seven-day arcs in the corpus with no observed integration failures (manifest tally: 24,641 ok / 0 failed).

The Earth-gravity-parameter convention differs between the SGP4/TLE stack and the EGM2008 force model: SGP4 uses WGS-72 ($\mu = 398,600.8 \text{ km}^3/\text{s}^2$, $R_{\oplus} = 6378.135 \text{ km}$), whereas EGM2008 uses the more recent WGS-84 values ($\mu = 398,600.4418 \text{ km}^3/\text{s}^2$, $R_{\oplus} = 6378.137 \text{ km}$). The fractional offset $\delta\mu/\mu \approx 1 \times 10^{-6}$ aliases into a semi-major-axis bias of similar order ($\mathcal{O}(10) \text{ m}$ at LEO) when the SGP4-derived state is re-interpreted as an EGM2008-osculating initial condition — not load-bearing for the kilometre-scale errors characterised in this paper, but cited explicitly here so the constant mismatch does not look unacknowledged.

3.7 Frame and time conventions

TEME (True Equator, Mean Equinox of date) is the pseudo-inertial frame in which SGP4 evaluates its mean-element ephemeris. Unlike J2000 or ICRF, TEME’s polar axis is the true equator of date and its origin in right ascension is the *mean* equinox; the resulting frame is approximately equivalent to J2000 ECI for short propagation arcs but accumulates a few milliarcseconds per year of drift due to nutation neglect in the right-ascension reference. Two conventions of TEME appear in the literature — the modern Vallado formulation, used here and implemented in the IAU SOFA / `erfa` stack, and an older STK “true-of-date” variant [Vallado, 2013, § 3.7]; we adopt the Vallado/erfa convention, which is the community-canonical choice for open-source TLE tooling. GMAT’s MJ2000Eq frame is the J2000 mean-equator / mean-equinox inertial frame — equivalent to “J2000 ECI” in non-GMAT vocabulary — and is the inertial frame the high-fidelity propagator integrates in.

Initial states for the GMAT propagation are derived from the starting TLE by evaluating SGP4 at $\Delta t = 0$ in TEME and rotating into MJ2000Eq. The TEME-to-MJ2000Eq rotation follows Algorithm 24 of Vallado [2013], composed from three primitives in the IAU SOFA / `erfa` library: the IAU 1976 precession matrix (`pmat76`), the IAU 1980 nutation matrix (`nut80` together with `numat`), and the 1994 equation of equinoxes (`eqeq94`). The underlying UTC \rightarrow TT transform is supplied by an IERS-aware time module referencing the Petit and Luzum [2010] conventions. The same rotation matrix is applied to the velocity vector; the residual error from neglecting $d\mathbf{M}/dt$ in the velocity rotation is bounded above by the precession rate ($\lesssim 50'' \text{ yr}^{-1}$) and the peak nutation amplitude ($\lesssim 9''$), translating to $\lesssim 10^{-5} \text{ mm s}^{-1}$ at LEO orbital speeds — several orders of magnitude below the kilometre-scale position errors characterised in this paper. SGP4 itself is evaluated through the `sgp4` Python implementation of Rhodes [2024], the canonical port of the Vallado open-source reference code, which uses the WGS-72 gravity constants that the TLE format was constructed against.

3.7.1 Dynamical-consistency caveat

The Cartesian state delivered by SGP4(TLE, $\Delta t = 0$) is *not* an osculating Cartesian state in the sense an external high-fidelity propagator expects. SGP4 is an analytic averaged-element propagator built on the Brouwer mean-element formulation [Vallado, 2013, § 11.6]: a TLE encodes mean Keplerian elements at epoch, and SGP4’s analytic kernel [Hoots et al., 2004] unwraps those mean elements through short-period perturbation series to produce a Cartesian position–velocity pair. That pair is a pseudo-osculating intermediate, not the instantaneously osculating state of the underlying physical orbit. Numerically integrating it as if it were osculating — as we do when feeding it to GMAT — carries the SGP4 short-period kernel’s intrinsic amplitude into the initial condition, bounded below by the short-period perturbation scale of order $\mathcal{O}(1) \text{ km}$ at LEO. The mismatch is fundamental to the comparison this paper performs: the high-fidelity arm inherits an initial condition that lives in a different dynamical reference than the truth construction (which re-evaluates SGP4 at the matched ending TLE), so part of the hi-fid-vs-SGP4 gap reported in Section 4 is the cost of leaving the SGP4 mean-element manifold rather than a deficiency of the integrator. This is one of the three mechanisms behind the H2 negative result discussed in Section 5.

3.8 Error metrics and solar context

For each sweep run we compute two position-error vectors at the end epoch t_j , both in MJ2000Eq. The first, $\Delta \mathbf{r}_{\text{SGP4}}$, is the difference between the state obtained by propagating the starting TLE with SGP4 to t_j and the proxy truth (next-TLE state) at t_j , constructed by evaluating SGP4 at $\Delta t = 0$ on the matched ending

TLE. The second, $\Delta\mathbf{r}_{\text{hifi}}$, is the corresponding difference for the GMAT high-fidelity propagation initialised from the same starting state in MJ2000Eq. The L_2 norms $\|\Delta\mathbf{r}_{\text{SGP4}}\|$ and $\|\Delta\mathbf{r}_{\text{hifi}}\|$ drive the staleness curves of Figures 2 and 3, the per-pair paired-scatter of Figure 5, and the per-cell power-law fits of Figure 4 and Table 5.

We additionally decompose each error vector into radial, along-track, and cross-track components in the local orbital frame of the next-TLE proxy at t_j . The basis follows the standard RSW construction [Vallado, 2013, §3.4]: $\hat{\mathbf{e}}_r = \hat{\mathbf{r}}_{\text{truth}}$; $\hat{\mathbf{e}}_h = \widehat{(\mathbf{r} \times \mathbf{v})}_{\text{truth}}$, along the angular-momentum direction (cross-track); and $\hat{\mathbf{e}}_t = \hat{\mathbf{e}}_h \times \hat{\mathbf{e}}_r$, completing the right-handed triad (along-track; approximately the velocity direction for the near-circular orbits in our corpus). The decomposition separates phase-only mistrack along the velocity direction from genuine geometric error in the plane perpendicular to it, and is the natural frame in which to compare propagator skill component by component; results are reported in Figure 6.

Each output row also carries the daily observed F10.7 solar flux and the planetary daily Ap index for the UTC date of the starting-TLE epoch, parsed from CelesTrak’s `sw19571001.txt` space-weather archive and cached locally in `src/static/sw_cache.parquet`. These two columns are post-processing analysis annotations used only by the H3 regression of the per-satellite SGP4 staleness coefficient against solar activity (Figure 7); they play no role in the integration itself, which reads its own space-weather inputs through GMAT’s bundled NRLMSISE-00 implementation (Section 3.6).

The CSSI space-weather inputs consumed by GMAT’s NRLMSISE-00 driver are read from a project-local snapshot of CelesTrak’s `sw19571001.txt` (Section 3.9), so the hi-fid integrator sees the same daily-observed $F_{10.7}$ and A_p values over the analysis window as the per-row annotation described above.

3.8.1 Statistical estimators

The per-cell power-law fit reported in Figure 4 and Table 5 is a weighted-with-unit-weights ordinary-least-squares regression of $\log_{10}\|\Delta\mathbf{r}\|$ on $\log_{10}(\Delta t/1\text{ h})$, fit on every pair in the (altitude shell \times pooled generation \times propagator) cell.

Each pair contributes its own measured Δt (the `actual_dt_sec` column of the per-run parquet, which carries the realised epoch spacing inside the ± 2 h matching tolerance); the four nominal staleness buckets {6 h, 1 d, 3 d, 7 d} used by Figures 2, 3, and 6 are a visualisation device only and do not enter the fit. A well-populated cell carries $\mathcal{O}(10^3)$ pairs, so the regression has $\mathcal{O}(10^3)$ degrees of freedom, not the four that a naive reading of the bucketed figures would suggest; per-pair fitting also lets the within-bucket spread in Δt contribute information that a fit to per-bucket medians would discard.

Per-pair weights are uniform: `pair-level SE(log10||Δr||)` is not available on the run parquet, and the satellite-level bootstrap introduced below absorbs the population scatter that an inverse-variance scheme would otherwise track.

Confidence intervals for A and k are percentile intervals from a 1,000-resample bootstrap drawn at the satellite level: each resample picks satellites with replacement from the cell and pools all four bucket-of-pairs from each drawn satellite. Resampling at the satellite rather than the pair level preserves within-satellite correlation across the four staleness buckets — pairs sharing a ballistic coefficient, attitude duty cycle, and perturbation history are not independent observations, and a pair-level bootstrap would understate uncertainty by treating them as such. Reported CIs are correspondingly tight on well-populated cells because $n \approx 167$ satellites per shell sample a geometrically narrow (a, e, i) neighbourhood, not because the resample under-accounts for the within-satellite covariance the construction specifically targets; the mixed-effects cross-check in Appendix F verifies that the parametric slope agreement holds across cells. Asymmetric percentile intervals are reported as such; bias-corrected and accelerated (BCa) intervals are not adopted as a default because the percentile intervals are visually symmetric in every populated cell, but the same satellite-level resampling is BCa-ready and could be swapped if a future re-run developed a skewed estimator.

Table 5 additionally reports the per-cell coefficient of determination R^2 of the unconstrained per-pair fit and likelihood-ratio test (LRT) p-values for the two physically interpretable nulls $k = 1$ (constant mean-motion bias, linear along-track displacement) and $k = 2$ (constant unmodelled along-track acceleration, quadratic along-track displacement). The LRT statistic for the slope constraint $k = k_0$ is the asymptotically χ_1^2 quantity $n \log(\text{RSS}_c/\text{RSS}_u)$, where RSS_u is the residual sum of squares of the unconstrained fit and RSS_c is the analogous quantity under $k = k_0$ with the intercept profiled out by recentering on $y - k_0x$. The LRT p-value is the survival probability of the test statistic under that asymptotic distribution. We do *not*

report bootstrap CIs for R^2 or for the LRT p-values: both are reported as point estimates from the full-cell unconstrained fit, since they answer questions about the goodness-of-fit and the discriminability of the slope nulls rather than about the fitted parameter values themselves.

Appendix F reports a parametric cross-check of the main estimator: a per-cell linear mixed-effects fit of $\log_{10}\|\Delta\mathbf{r}\|$ on $\log_{10}\Delta t$ with a satellite-level random intercept, $\log_{10}\|\Delta\mathbf{r}\| \sim \log_{10}\Delta t + (1 \mid \text{norad_id})$. Mixed effects treat the same within-satellite correlation parametrically, by assuming a normal random-intercept distribution across satellites; the bootstrap handles it non-parametrically. A substantive disagreement between the two on any cell would be a signal to escalate the mixed-effects fit to the primary estimator in a follow-up revision. The per-cell comparison and a mixed-effects-versus-bootstrap agreement summary are deferred to the appendix so the main-body table remains the single estimator of record.

3.8.2 Physical interpretation of the power-law exponent

The power-law form $\|\Delta\mathbf{r}(\Delta t)\| \approx A\Delta t^k$ is descriptive rather than first-principles, but its two physically interpretable limits $k = 1$ and $k = 2$ that the LRT in Section 3.8.1 tests against correspond to specific error-source regimes in the orbit-propagation budget, both expressed through the along-track component on which the gross error overwhelmingly lives (Section 4 and Figure 6).

Consider first a constant mean-motion error δn at epoch — the operational footprint of a B^* mis-fit, where the operator-fitted ballistic coefficient at t_i encodes a mean drag environment over the OD window that differs systematically from the conditions encountered during forward propagation. Integrating the rotational equation $\dot{\theta} = n + \delta n$ over $(t_i, t_j]$ gives an along-track angle offset $\delta\theta = \delta n\Delta t$, which maps to an arc-length displacement

$$\Delta s(\Delta t) \approx a\delta n\Delta t, \quad (2)$$

i. e. $k = 1$ with $A = a\delta n$ (in suitable units for the $\Delta t = 1$ h normalisation Table 5 adopts). The displacement is linear in Δt because the mean-motion error is constant; no integration of an acceleration is involved.

Consider now a constant unmodelled in-track acceleration a_{res} — the operational footprint of a drag-area or spacecraft-property mis-specification, where the integrator (or, implicitly, SGP4’s own averaged drag term) sees a $\rho C_D A$ product offset from the truth by a constant. Integrating $\ddot{s} = a_{\text{res}}$ twice with zero displacement and velocity at t_i gives

$$\Delta s(\Delta t) \approx \frac{1}{2}a_{\text{res}}\Delta t^2, \quad (3)$$

i. e. $k = 2$ with $A = a_{\text{res}}/2$ (again in $\Delta t = 1$ h units).

The empirical k values across our populated cells span both sides of unity — Table 5 reports k between 0.75 and 1.44 across the SGP4 cells and k between 0.99 and 1.28 across the high-fidelity cells — which is the expected signature of a *mixture* of the two error modes operating simultaneously: a partial B^* mis-fit at epoch dragging k toward unity (Eq. (2)) and a residual constant-acceleration term dragging it toward two (Eq. (3)), with the cohort-specific balance between them setting the per-cell exponent. The per-cell (A, k) pair is, on this reading, a coarse two-parameter summary of the operator’s epoch-time error budget for that satellite cohort: A scales with the joint magnitude of both contributions evaluated at $\Delta t = 1$ h, and k encodes the mix — closer to unity when mean-motion bias dominates, closer to two when a residual constant in-track acceleration dominates. Other contributions (initial-state error mapped forward by the state transition matrix, time-varying drag through a non-constant ρ , gravity-truncation residuals) shift the effective (A, k) pair without changing the two limiting endpoints; the LRT in Section 3.8.1 discriminates a cell against those endpoints with the same χ_1^2 statistic in both directions.

3.8.3 H3 regression specification

Hypothesis H3 asks whether the per-satellite SGP4 staleness coefficient A_i tracks the solar-EUV proxy F10.7 in the drag-dominant cohorts of the corpus. The model choice follows from a short derivation. Atmospheric drag at LEO is $\mathbf{a}_{\text{drag}} = -\frac{1}{2}\rho(h, \text{F10.7})v^2(C_D A/m)\hat{\mathbf{v}}_{\text{rel}}$; SGP4 absorbs the time-averaged $\frac{1}{2}(C_D A/m)\rho_{\text{ref}}$ encountered during the OD window into a single fitted scalar B^* , so the operator’s epoch-time fit lags actual density whenever F10.7 trends within the prediction span. The forward-propagation along-track error from that lag is proportional to $\Delta\rho(\text{F10.7})/\rho_{\text{ref}}$ integrated over Δt . Taking logs of the underlying multiplicative chain,

$$\log_{10}A_i \approx \log_{10}(C_D A/m)_i + \log_{10}\rho_{\text{ref}}(h_i, \text{F10.7}_i) + \text{const}, \quad (4)$$

and differentiating in F10.7 at fixed altitude isolates the quantity H3 is asking about:

$$\left. \frac{\partial \log_{10} A}{\partial \text{F10.7}} \right|_h = \left. \frac{\partial \log_{10} \rho}{\partial \text{F10.7}} \right|_h. \quad (5)$$

Spacecraft properties enter the intercept of Eq. (4) through the per-satellite ($C_D A/m$) term, but they drop out of Eq. (5) entirely. The H3 slope is therefore predicted to be a function of altitude and the local density-modulation kernel only, and not of platform generation.

We accordingly fit one slope per altitude shell, with the intercept differences between pooled generations absorbed as a nuisance covariate. The model is the additive ANCOVA form

$$\log_{10} A_i = \alpha_{\text{gen}(i)} + \beta \text{F10.7}_i + \varepsilon_i, \quad (6)$$

fit by ordinary least squares per shell. The A_i entering Eq. (6) is the per-satellite SGP4 power-law coefficient recovered by the Section 3.8.1 fit restricted to a single satellite. The fit is restricted to the SGP4 arm because the operator-fitted B^* is the quantity Eq. (5) concerns; a parallel hi-fid regression on $A_{i,\text{hi-fid}}$ is a natural follow-up.

The naive alternative — a per-shell pooled fit that drops the α_{gen} term — fails empirically at 550 and 560 km. The v1.x and v2-mini cohorts share an altitude shell but carry per-satellite A medians that differ by roughly a factor of four (v1.x at 0.13–0.22, v2-mini at 0.06 km at $\Delta t = 1$ h), reflecting the larger $C_D A/m$ scale of the newer bus together with operator OD differences across the two generations. Their epoch distributions also sample slightly different mean F10.7 within the analysis window. A pooled 550 km regression that ignores the intercept gap aliases that cross-cohort offset into a wrong-signed slope: $\hat{\beta} = -0.054$ per sfu at $p \approx 2 \times 10^{-7}$, diagnostic-run on the same corpus. The ANCOVA form of Eq. (6) absorbs the offset into α_{gen} and exposes the within-cohort slope that Eq. (5) actually predicts.

For each shell we additionally fit the interaction-augmented model $\log_{10} A_i = \alpha_{\text{gen}(i)} + (\beta + \delta \beta_{\text{gen}(i)}) \text{F10.7}_i + \varepsilon_i$ and report the partial- F test of $H_0: \delta \beta_{\text{gen}} = 0$ against the additive model. Under Eq. (5) the additive restriction is the physics expectation; rejection of H_0 is informative as a sign that the simple drag-mismodelling picture omits a cohort-specific F10.7 response we have not modelled, not as a license to substitute the interaction model as the headline estimator.

Two predictors are reported per shell. The headline predictor is the per-satellite mean of the daily observed F10.7 over the satellite’s window of starting epochs, parsed from the CelesTrak cache described in Section 3.8. As a robustness check we additionally fit Eq. (6) with the per-satellite mean of the CelesTrak 81-day-centred F10.7 average as the predictor; the 81-day average is the long-term thermospheric driver that NRLMSISE-00 consumes internally and is the convention-matched predictor for any attempt to interpret $\hat{\beta}$ as a density-modulation slope.

Over the 30-day corpus window the daily-mean predictor spans roughly 17 sfu sat-to-sat (≈ 104 –138), while the 81-day-centred predictor compresses to ≈ 1.3 sfu (≈ 124.6 –125.9) by construction. The 81-day robustness fit has very limited statistical leverage on the present window, so we treat the daily-mean fit as the load-bearing report.

For each (shell, predictor) cell the full-sample OLS of Eq. (6) gives the point estimates ($\hat{\alpha}_{\text{gen}}, \hat{\beta}$) with asymptotic standard errors $\text{SE}(\hat{\beta})$ and the two-sided t -stat p -value for $H_0: \beta = 0$ under standard OLS assumptions on the residuals. The 95% percentile confidence interval on $\hat{\beta}$ is taken from a 1,000-resample satellite-level bootstrap that draws sats with replacement from the shell and refits the additive model; CI bounds are the 2.5th and 97.5th percentiles of the resampled $\hat{\beta}$ distribution. The same bootstrap supplies per-gen intercept-offset CIs through the resampled $\hat{\alpha}_{\text{gen}}$ values, so the figure’s per-gen CI ribbons combine the slope and intercept-offset uncertainties consistently. The resampling structure is identical to that of the per-cell power-law CIs in Section 3.8.1.

Empirical results are reported in Figure 7 and discussed in Section 5. The daily-mean fit returns, per shell:

- 540 km (v1.x only): $\hat{\beta} = +0.017$ per sfu (95% CI $[-0.002, +0.036]$, $p = 0.07$, $R^2 = 0.02$).
- 550 km (v1.x, v2-mini): $\hat{\beta} = -0.009$ per sfu (95% CI $[-0.029, +0.009]$, $p = 0.31$, $R^2 = 0.45$), with the slope consistent with zero and the interaction test failing to reject the additive model ($p_{\beta \times \text{gen}} = 0.69$).

- 560 km (v1.x, v2-mini): $\hat{\beta} = +0.014$ per sfu (95% CI [+0.001, +0.031], $p = 0.034$, $R^2 = 0.24$) — the smallest positive slope to clear conventional significance on this corpus.

The high R^2 values at 550 and 560 km reflect the intercept covariate absorbing the cross-cohort baseline gap, not an explanatory contribution from F10.7. The interaction test at 560 km does reject the additive restriction ($p_{\beta \times \text{gen}} = 0.005$); the narrow predictor span and modest cell counts make the departure from Eq. (5) difficult to attribute cleanly to either a real cohort-specific F10.7 response or to a window-end sampling pattern, and we flag it rather than re-fit.

The 81-day-centred robustness fits, refit on the same shells with the same ANCOVA design, return $\hat{\beta} = +0.003$ per sfu (95% CI [-0.296, +0.241], $p = 0.98$) at 540 km, $\hat{\beta} = -0.432$ per sfu (95% CI [-0.703, -0.205], $p = 0.001$) at 550 km, and $\hat{\beta} = -0.253$ per sfu (95% CI [-0.473, +0.008], $p = 0.015$) at 560 km. The negative slopes at 550 and 560 km are physically wrong-signed — the local $\partial \log \rho / \partial \text{F10.7}$ at LEO altitudes is uniformly positive, so a genuine drag-modulation signal would return $\hat{\beta} > 0$ — and we read the apparent significance as a sampling artefact rather than a competing H3 estimate. The 1.3 sfu pooled span of the 81-day-centred predictor compresses within each cohort to 0.57–1.24 sfu, narrow enough that each satellite’s per-sat mean is set largely by which sub-window of April 2026 its starting epochs cluster in; any window-internal correlation between epoch placement and per-sat A then maps into the slope rather than into the α_{gen} covariate. We report the 81-day fits for completeness and treat the daily-mean fit as the load-bearing H3 estimate on the present 30-day corpus.

Section 5 returns to whether the absence of a clear $|\hat{\beta}_{540}| \gtrsim |\hat{\beta}_{560}|$ altitude-attenuation ordering reflects a genuine cohort-level cancellation or the narrowness of the F10.7 lever available in the analysis window.

3.9 Reproducibility surface

The source repository contains the complete data-preparation pipeline (TLE fetch, sampling, pair construction, maneuver filter, spacecraft-property attachment), the GMAT mission script, the parallel sweep driver, the aggregation and statistics utilities, every figure-generation script, and the manuscript L^AT_EX source, all released under the MIT licence at the URL given in Section F. The sweep output bundle — per-run parquets, the resumable manifest, and the mission script used to generate them — is deposited on Zenodo at the version DOI listed in the build configuration; the manuscript build target fetches that bundle and rebuilds every figure from the cached data, so re-rendering the PDF from a clean checkout does not require a local GMAT installation. Re-running the full sweep from scratch does require GMAT R2026a, the EGM2008 coefficient file installed through the project’s installer script, and Space-Track credentials for the one-time TLE fetch.

The CSSI-format space-weather text file consumed by GMAT’s NRLMSISE-00 driver is committed as a frozen snapshot of CelesTrak’s `sw19571001.txt` in the repository under `src/static/SpaceWeather-All-v1.2.txt`; it is regeneratable from the CelesTrak source via `make fetch-gmat-sw`. The sweep driver supplies the snapshot’s absolute path to GMAT through the `FM.Drag.CSSISpaceWeatherFile` script-level override, so the integrator reads observed daily $F_{10.7}$ and A_p values over the entire analysis window rather than the predicted inputs that GMAT R2026a’s shipped CSSI file would supply for epochs past its observed-data horizon. The committed snapshot covers the April 2026 corpus window with daily observed data through 2026-05-16.

Exact versions of the load-bearing astrodynamics dependencies — SOFA / `erfa` for the TEME-to-MJ2000Eq rotation, the `sgp4` Python implementation of Rhodes [2024] for the SGP4 evaluation, and `astropy` for IERS-aware time conversion — are pinned in `pyproject.toml` and the conda environment lockfile shipped in the repository, so the rotation chain and SGP4 numerical kernel are bit-identical across re-runs.

4 Results

The locked sweep retired with 24,641 ($\text{TLE}_i, \text{TLE}_j$) pairs distributed across 501 Starlink satellites and the four target staleness offsets $\Delta t \in \{6, 24, 72, 168\}$ h; the GMAT manifest reports 24,641/24,641 propagations completed with zero integration or preprocessing failures. The per-(altitude shell \times generation) composition of the surviving corpus is the one already given in Table 2, and the geometric coverage of the sampled satellites in the three Keplerian shape elements (a, e, i) is shown in Figure 1: the three near-vertical bands in semi-major axis reproduce the operational altitude shells to within the per-satellite station-keeping band;

eccentricity is bounded at $\lesssim 4 \times 10^{-4}$ across the entire sample (the operational near-circular signature of an actively phase-controlled fleet); and inclination clusters at the documented 43° , 53° , 70° , and 97° deployment lanes, with v1.0 confined to the 53° Group 1 shells, v1.5 spanning 43° and 53° , and v2-mini populating the newer 43° , 70° , and 97° shells. The geometric narrowness of the corpus in (a, e) matters downstream: the per-cell comparisons reported in Sections 4.1–4.4 contrast propagator skill at near-identical orbit geometry, so any inter-cell differences are attributable to atmosphere and platform properties rather than to gross variation in dynamical regime.

We organise the reading of Section 4 around the three hypotheses of Section 1. Pooled across the 24,641 corpus pairs, the L_2 position error against the next-TLE proxy grows from a median of 0.94 km (SGP4) / 1.49 km (high-fid) at the 6 h horizon to 11.7 / 24.5 km at 3 d and 38.5 / 76.0 km at 7 d. Section 4.1 parametrises that growth into the staleness curves of H1; Section 4.2 contrasts the two propagators pair by pair (H2); Section 4.3 resolves the position-error vector into its radial, along-track, and cross-track components; and Section 4.4 regresses the per-sat staleness coefficient against the daily F10.7 flux to test H3.

4.1 Staleness curves and power-law fits (H1)

Figures 2 and 3 show the per-bucket median position error and its 25th–75th percentile band, by altitude shell, on identical log-log axes and identical y -limits so the SGP4-vs-high-fid visual comparison is honest. Within the v1.x panel the curves separate mildly with altitude (the 540 km shell carries the largest median at every Δt , consistent with drag dominance at the lowest altitude in the corpus); within the v2-mini panel the two populated shells collapse, the dominant offset being inter-cohort rather than inter-shell. Walking the v1.x cells from $\Delta t = 6$ h upwards, the SGP4 median grows from 1.01 km (550 km shell) to 2.60, 5.64, and 15.67 km at 1, 3, and 7 d respectively; the high-fidelity arm tracks the same curve shape at the same shell but sits a factor of 1.6–3.6 higher across the four buckets, and is uniformly above SGP4 on v1.x across the corpus. The pattern partially carries over to v2-mini — SGP4 itself grows more steeply (0.96 \rightarrow 4.53 \rightarrow 25.11 \rightarrow 101.71 km on the SGP4 arm at the 550 km shell) — but the ordering of the two medians flips with Δt : the high-fidelity arm sits above SGP4 at 6 h and 1 d but falls *below* SGP4 at 3 d (23.3 vs. 25.1 km) and 7 d (72.3 vs. 101.7 km) on the 550 km v2-mini cell, and at 7 d (84.5 vs. 89.8 km) on the 560 km v2-mini cell. The cohort-level pattern from the per-bucket aggregates — high-fid uniformly above SGP4 on v1.x, crossing over below SGP4 on the long- Δt v2-mini cells — previews the pair-by-pair H2 reading of Section 4.2.

The curves are well-fit by the H1 form $\|\Delta \mathbf{r}(\Delta t)\| \approx A \Delta t^k$ at the per-pair level (Section 3.8.1). Figure 4 renders the fitted parameters per (altitude shell \times pooled generation) cell with 95% satellite-level bootstrap CIs; the numerical values are listed in Table 5. Three patterns survive the bootstrap. First, on the v1.x cohort SGP4 yields a sub-linear exponent (\hat{k} ranges from 0.75 [0.69, 0.83] at 550 km through 0.84 [0.82, 0.87] at 540 km to 0.86 [0.82, 0.89] at 560 km), while the high-fidelity arm on the same cohort spans 0.99 [0.95, 1.04] at 550 km (where \hat{k} sits at the $k = 1$ boundary and the CI straddles it), 1.12 [1.08, 1.15] at 560 km, and 1.28 [1.26, 1.30] at 540 km. The likelihood-ratio test rejects both the $k = 1$ and $k = 2$ nulls at $p < 10^{-3}$ in every populated cell except the high-fidelity v1.x cell at 550 km, where the $k = 1$ null is not rejected ($p_{k=1} = 0.76$, Table 5) and the cell sits in the mean-motion-bias limit of Section 3.8.2. Elsewhere the mixture interpretation, with \hat{k} encoding the relative weight of a B^* mean-motion bias versus a constant unmodelled along-track acceleration, is the physically consistent reading. Second, the two propagators trade A for k in opposite directions across the v1.x cells: high-fid carries the smaller (or equal) coefficient at the $\Delta t = 1$ h normalisation point (the bolded entries of Table 5) but the steeper slope, so the two staleness curves cross within the corpus window and the v1.x gap of Figures 2–3 widens with Δt . Third, the v2-mini cohort is super-linear under *both* propagators (\hat{k} between 1.15 and 1.44), with the unusual feature that SGP4 carries the smaller coefficient *and* the steeper slope at both shells, so on v2-mini it is the high-fidelity arm that becomes the slower-growing curve and the two staleness curves cross with SGP4 climbing past high-fid by 3 d — the §4.1-paragraph statement of the v2-mini crossover that drives the H2 reading in Section 4.2.

H1 is therefore not merely supported but *quantified*: every populated cell of the corpus carries a statistically distinguishable power-law staleness curve, the per-cell (A, k) pair varies systematically and interpretably across (shell \times generation), and the cohort-specific values of Table 5 are the practitioner-facing summary the analysis is built to provide. The behaviour above the truth-floor regime of Section 2.1 — $\Delta t \gtrsim 1$ d, where the

Table 5: Power-law fit parameters per (altitude shell \times pooled generation), for SGP4 and high-fidelity propagators. Values for the coefficient A and exponent k are point estimates from the per-pair OLS fit (Section 3.8.1) followed by the 95% satellite-level bootstrap CI. R^2 is the coefficient of determination of the unconstrained per-pair fit; the $p_{k=1}/p_{k=2}$ column reports the likelihood-ratio-test p-values for the two slope nulls $k = 1$ and $k = 2$. Per row, the A entry of whichever propagator has the smaller fitted coefficient is bolded; this is the propagator with the lower error at the $\Delta t = 1$ h normalisation point, not necessarily at the longer bucket centres.

shell	generation	SGP4				high-fid			
		A [95% CI]	k [95% CI]	R^2	$p_{k=1}/p_{k=2}$	A [95% CI]	k [95% CI]	R^2	$p_{k=1}/p_{k=2}$
540 km	v1.x	0.19 [0.17, 0.2]	0.84 [0.82, 0.87]	0.40	$<10^{-3} / <10^{-3}$	0.13 [0.12, 0.14]	1.28 [1.26, 1.30]	0.68	$<10^{-3} / <10^{-3}$
550 km	v1.x	0.23 [0.19, 0.28]	0.75 [0.69, 0.83]	0.33	$<10^{-3} / <10^{-3}$	0.23 [0.19, 0.27]	0.99 [0.95, 1.04]	0.55	0.760 / $<10^{-3}$
550 km	v2-mini	0.049 [0.045, 0.053]	1.44 [1.42, 1.46]	0.77	$<10^{-3} / <10^{-3}$	0.15 [0.13, 0.18]	1.15 [1.10, 1.19]	0.67	$<10^{-3} / <10^{-3}$
560 km	v1.x	0.15 [0.13, 0.17]	0.86 [0.82, 0.89]	0.41	$<10^{-3} / <10^{-3}$	0.15 [0.13, 0.17]	1.12 [1.08, 1.15]	0.58	$<10^{-3} / <10^{-3}$
560 km	v2-mini	0.073 [0.066, 0.083]	1.32 [1.29, 1.35]	0.73	$<10^{-3} / <10^{-3}$	0.18 [0.16, 0.2]	1.15 [1.11, 1.18]	0.66	$<10^{-3} / <10^{-3}$

observed error climbs into double-digit kilometres and the OD-residual contribution becomes percent-level – carries the load-bearing fits; the 6 h cell is reported alongside for the operational completeness already documented in §3.3 but is interpreted in Section 5 against the Section 2.1 floor.

4.2 Pair-by-pair propagator comparison (H2)

The aggregate statistics of Section 4.1 compare medians; H2 asks the sharper pair-wise question: in what fraction of (TLE_i, TLE_j) pairs is the high-fidelity $|\Delta \mathbf{r}|$ smaller than the SGP4 $|\Delta \mathbf{r}|$ against the same proxy truth? Figure 5 plots every pair on the $(|\Delta \mathbf{r}_{\text{SGP4}}|, |\Delta \mathbf{r}_{\text{hifi}}|)$ plane, broken out by altitude shell (columns) and Δt bucket (rows). Each panel’s lower-right annotation reports the fraction of pairs sitting below the $y = x$ diagonal (“hi-fid wins”); the bootstrap-quantified per-cell version of that fraction, together with the along-track-only variant $|\Delta r_{\text{along, hifi}}| < |\Delta r_{\text{along, SGP4}}|$ that Figure 6 below motivates as the natural metric in the long- Δt regime, is given in Table 6.

Pooled across all cells, the high-fidelity arm beats SGP4 on 33.7% [32.2, 35.3] of 6 h pairs in 3D L_2 norm, 25.1% [23.9, 26.1] at 1 d, 28.7% [26.6, 30.9] at 3 d, and 35.3% [31.9, 38.8] at 7 d. The non-monotone pooled trajectory — worst at 1 d, recovering toward the 6 h fraction by 7 d — masks a strong per-cell pattern that Table 6 resolves below. The along-track variant sits within sampling error of the L_2 variant at every horizon except 6 h, where it climbs to 36.0% [34.3, 37.6]: at the shortest horizon the cross-track and radial components of $\Delta \mathbf{r}$ are still appreciable contributions to the L_2 norm (see Section 4.3 below), while at ≥ 1 d the L_2 comparison is already an along-track comparison in disguise, and the two metrics return the same fraction within the bootstrap CI. Either way SGP4 wins on ~ 65 –75% of pairs across the corpus, which is the per-pair statement of the H2 negative finding.

The per-cell decomposition exposes a strong cohort dependence behind the pooled numbers. At 540 km the high-fidelity-wins fraction collapses from 34.6% [32.3, 36.8] at 6 h to 5.4% [3.9, 7.0] at 7 d: as Δt grows the high-fidelity arm at the lowest shell saturates against a propagation floor visible in Figure 5 as the “ $|\Delta \mathbf{r}_{\text{hifi}}|$ horizontal band” centred near 100–200 km in the 3 d and 7 d panels, while the SGP4 distribution remains spread over three decades. That signature is the joint fingerprint of a near-constant force-model bias on the high-fidelity arm (drag mismodelling on the lowest-altitude cohort) and a wider operator-OD-residual distribution on SGP4 – the combination yields a stripe of paired points whose ordinate is nearly Δt -determined and whose abscissa varies. At 550 km the shell-level high-fidelity-wins fraction is qualitatively different: it climbs with Δt from 39.8% [37.0, 42.6] at 6 h to 60.2% [55.9, 64.4] at 7 d, the only shell-level cell of the corpus where the high-fidelity arm beats SGP4 on a majority of pairs. At 560 km the comparable shell-level wedge is weaker — the cell’s 7 d high-fidelity-wins fraction is 26.7% [22.1, 31.6] — suggesting at first reading that the 550 km flip is an isolated exception.

That reading is partly an artefact of cohort blending in the shell-level statistic. The 550 km \times 7 d cell is 78% v2-mini by pair count whereas the 560 km \times 7 d cell is only 34% v2-mini, so the same per-cohort behaviour projects very differently onto the shell-level wins fraction when the v1.5 majority drags the 560 km number down. The cohort-resolved fractions in Table 8 (in Section 5.2) make the point directly: on the v2-mini cohort alone the high-fidelity arm wins 72.6% [69.9, 75.4] of 7 d pairs at 550 km and 55.1% [49.9, 60.4]

Table 6: Per-cell fraction of (TLE_i, TLE_j) pairs on which the high-fidelity propagator achieves a smaller position error than SGP4 against the next-TLE proxy. The 3D L_2 column reads “ $\|\Delta\mathbf{r}_{\text{hifi}}\| < \|\Delta\mathbf{r}_{\text{SGP4}}\|$ ” (the metric underlying Figure 5); the along-track column reads “ $|\Delta r_{\text{along, hifi}}| < |\Delta r_{\text{along, SGP4}}|$ ” on the RSW component of Figure 6. Both fractions carry 95% satellite-level percentile bootstrap CIs (1,000 resamples drawing satellites with replacement and pooling all of each drawn satellite’s pairs in the cell; identical resampling structure to Table 5). Per-cell rows with fewer than 30 pairs are suppressed; pooled-per- Δt rows aggregate across all shells and generations. The cohort-resolved decomposition of these rows (per-shell \times Δt \times generation) win fractions) is in Table 8 alongside the Section 5.2 cohort-mechanism discussion.

Shell (km)	Δt	n_{pairs}	hi-fid wins, 3D L_2 [95% CI]	hi-fid wins, along-track [95% CI]
540	6h	1,957	34.6% [32.3, 36.8]	35.6% [33.2, 37.8]
540	1d	2,854	17.6% [16.2, 19.1]	17.5% [16.1, 19.1]
540	3d	1,748	6.5% [5.4, 8.0]	6.5% [5.4, 8.0]
540	7d	920	5.4% [3.9, 7.0]	5.4% [3.9, 7.0]
550	6h	2,031	39.8% [37.0, 42.6]	42.8% [39.9, 45.8]
550	1d	3,351	30.3% [28.8, 31.9]	30.4% [28.9, 31.9]
550	3d	2,587	45.1% [42.0, 47.9]	45.1% [42.0, 47.9]
550	7d	1,562	60.2% [55.9, 64.4]	60.2% [55.9, 64.4]
560	6h	1,433	23.9% [21.3, 26.5]	26.8% [24.1, 29.4]
560	1d	2,725	26.4% [24.5, 28.4]	26.3% [24.4, 28.4]
560	3d	2,124	27.0% [24.3, 30.1]	26.9% [24.2, 30.1]
560	7d	1,349	26.7% [22.1, 31.6]	26.6% [21.9, 31.6]
<i>pooled</i>	6h	5,421	33.7% [32.2, 35.3]	36.0% [34.3, 37.6]
<i>pooled</i>	1d	8,930	25.1% [23.9, 26.1]	25.0% [23.9, 26.1]
<i>pooled</i>	3d	6,459	28.7% [26.6, 30.9]	28.7% [26.6, 30.9]
<i>pooled</i>	7d	3,831	35.3% [31.9, 38.8]	35.2% [31.9, 38.8]

of 7 d pairs at 560 km, both clearly above the 50% null; while on v1.x the arm loses badly at both shells (16.1% [11.0, 22.2] at 550 km; 11.9% [8.8, 15.5] at 560 km). The cohort signal at 7 d is therefore cohort-uniform, not shell-specific. The same table shows the v2-mini hi-fid-wins fraction rising with Δt at *both* populated shells from below half at 6 h to a majority at 7 d. Section 5.2 returns to the physical mechanism behind the cohort split.

H2 therefore holds with the reading: the high-fidelity propagator initialised from public TLEs does not improve on SGP4 in the bulk of the corpus, and the pooled win fraction is statistically distant from the 50% null at every Δt . The cohort-specific exception — v2-mini at long Δt , present at both 550 and 560 km — is the regime where the SGP4 cohort itself struggles most (super-linear $\dot{k} = 1.44$ and 1.32 respectively in Table 5), making even an inherently biased high-fidelity propagator competitive on a non-trivial fraction of pairs. Section 5 decomposes the bulk negative result into three distinct mechanisms, and Section 5.2 elaborates the cohort-resolved reading.

4.3 Error decomposition

Figure 6 resolves $\Delta\mathbf{r}$ into the standard radial, along-track, and cross-track components in the next-TLE-proxy RSW frame (Section 3.8). The along-track median sits a clean two decades above the cross-track and radial medians at every Δt bucket and in every populated cohort, and the gap widens with Δt . On the v1.x cohort, along-track grows roughly $1 \rightarrow 4 \rightarrow 6 \rightarrow 16$ km from 6 h to 7 d on the SGP4 arm; the v2-mini cohort grows $1 \rightarrow 4 \rightarrow 24 \rightarrow 98$ km on the same arm and reaches ~ 76 km at 7 d on the high-fidelity arm. Over the same horizons the cross-track and radial medians grow from $\mathcal{O}(0.03\text{--}0.1)$ km at 6 h to $\mathcal{O}(0.3\text{--}1)$ km at 7 d, two decades below the along-track band throughout. By $\Delta t = 7$ d, the L_2 norm of Figures 2–3 and the along-track component of Figure 6 are indistinguishable within the line widths of the figure: at the

long-staleness limit, the L_2 position error *is* the along-track error.

The decomposition gives the along-track-norm in operationally meaningful units: 1 km of along-track displacement at the 550 km shell’s circular speed $v_c \approx 7.59 \text{ km s}^{-1}$ corresponds to ~ 0.13 s of orbital phase, marked on the secondary axis of the along-track panel. The 6 h headline median of ~ 1 km from Section 4.1 is therefore a sub-orbit-second timing miss along the velocity direction, while the 7 d high-fidelity median of ~ 76 km corresponds to ~ 10 s of phase. Cross-track and radial components – bounded under the dominant LEO perturbations by orbital-period oscillation and second-order coupling [Vallado, 2013, § 3.4] – accumulate freely over neither horizon, and the SGP4 and high-fidelity dashed lines on those two panels overlay each other within the IQR ribbons. The H2 propagator gap is therefore an along-track gap; the discussion in Section 5.3 returns to why.

4.4 Solar modulation (H3)

H3 asks whether the per-satellite SGP4 staleness coefficient A_i of Section 3.8.1 tracks the daily-observed F10.7 flux in the most drag-sensitive cohorts. Figure 7 plots the per-sat A_i scatter against the per-sat mean of the CelesTrak daily F10.7 over the satellite’s window of starting epochs, one panel per altitude shell, and overlays the additive ANCOVA fit of Eq. (6) (one dashed line per generation present, sharing the fitted slope $\hat{\beta}$ across cohorts and absorbing inter-cohort offsets into $\hat{\alpha}_{\text{gen}}$ as predicted by Eq. (5)).

The headline daily-F10.7 ANCOVA fit returns one slope per shell, summarised in Table 7: a positive slope at 540 km that does not exclude zero at the corpus’s narrow predictor span (~ 17 sfu across satellites); a slope indistinguishable from zero at 550 km; and a positive slope at 560 km that clears conventional significance. The 560 km cell is therefore the only one where H3 modulation is statistically distinct from the null on the present 30-day window. The 540 km cell is direction-consistent with the textbook positive density gradient with F10.7 at LEO, but the intra-corpus F10.7 lever is too narrow to discriminate the predicted slope from zero on its own.

Table 7: Per-shell ANCOVA fit of Eq. (6) with the daily-observed F10.7 as predictor: slope estimate $\hat{\beta}$ in sfu^{-1} , 95% satellite-level percentile bootstrap CI, two-sided t -stat p -value for $H_0 : \beta = 0$, and model R^2 . The partial- F interaction test column reports the p -value of the F10.7 \times generation interaction against the additive restriction (shells with a single cohort have no such test). The intercept-offset column reports $\hat{\alpha}_{\text{v2-mini}} - \hat{\alpha}_{\text{v1.x}}$ for shells where both cohorts are present.

Shell (km)	n_{sats}	cohorts	$\hat{\beta}$ (sfu $^{-1}$)	95% CI (sfu $^{-1}$)	p	$\Delta\hat{\alpha}$ (log $_{10}$)
540	167	v1.x	+0.017	[−0.002, +0.036]	0.07	—
550	165	v1.x, v2-mini	−0.009	[−0.029, +0.009]	0.31	−0.54
560	156	v1.x, v2-mini	+0.014	[+0.001, +0.031]	0.034	−0.38
Interaction-vs-additive partial- F			F10.7 \times gen	p -value		
540				—		
550			additive ok	0.69		
560			additive rejected	0.005		

The 560 km interaction test does reject the additive restriction ($p = 0.005$), indicating a cohort-specific F10.7 response at that shell that Eq. (5) does not predict. The departure is flagged in Section 5 as either a real second-order effect of the v2-mini bus or a window-end sampling pattern interacting with the F10.7 trend over the analysis window; the additive headline slope at 560 km remains the $\hat{\beta}$ that Eq. (5) concerns directly, and we report it without substitution by the interaction model.

The 81-day-centred robustness fits, reported per-shell in Section 3.8.3, return slopes that are physically wrong-signed at 550 and 560 km (negative on a quantity whose thermospheric-density gradient is uniformly positive at LEO) and reach nominal significance only because the predictor’s ~ 1.3 sfu span across satellites is dominated by where in April 2026 each satellite’s starting epochs cluster rather than by a genuine solar-driver signal. We treat those fits as the limit-of-leverage diagnostic they are – documented in Section 3.8.3 alongside

the daily-mean fit – and the daily-mean $\hat{\beta}$ of Figure 7 as the load-bearing H3 report on the present 30-day corpus. H3 is therefore detectable in direction across the two cells where the analysis has discriminating power (positive $\hat{\beta}$ at 540 and 560 km, the two shells with the broadest within-cohort F10.7 lever) but is statistically distinct from zero only at one of them.

5 Discussion

The empirical headline of Section 4 — that the high-fidelity propagator initialised from a public TLE is behind SGP4 against the next-TLE proxy at every shell-pooled Δt bucket of the corpus, losing on 65–75% of pairs depending on horizon (Table 6) — supports a more specific reading than “high-fidelity propagation is wasted”. The load-bearing statement is the conditional one: *higher physical fidelity in the propagator does not imply superior predictive accuracy against next-TLE-derived truth when the initial condition is itself a state estimated under a different dynamical model*. The H2 gap is then not a property of the high-fidelity force model in isolation but of the joint (initial-state, truth-construction, force-model) triple that the public-TLE workflow imposes. Section 5.1 walks that joint object through three mechanisms whose dominance regimes partition the four Δt buckets cleanly between them; Section 5.2 resolves the bulk negative result by cohort and isolates the v2-mini long- Δt regime where high-fidelity propagation overtakes SGP4 on a majority of pairs; the along-track structure of the error budget (Section 5.3), the practitioner-facing quantitative verdict (Section 5.4), and the limitations and follow-ups (Sections 5.5–5.7) follow.

5.1 Three mechanisms behind the H2 gap

Mechanism 1 — Operator-OD residual dominance at short Δt . A useful sanity check on the 6 h headline number is to compare it directly with the truth-floor diagnostic of Section 2.1. Pooled across the eight cohort representatives the diagnostic returns a median L_2 residual of 1.11 km on a ~ 5 h short arc (per-cohort medians 0.81–1.37 km, Table 1), whereas the SGP4 pooled median at $\Delta t = 6$ h is below that value at ~ 0.94 km (Section 4.1). Two TLE-derived states separated by one operator update interval cannot agree better than the floor implied by their independent OD residuals; the only way the observed 6 h SGP4 number sits beneath the diagnostic floor is by partial cancellation between adjacent operator OD residuals — shared attitude assumptions, shared recent-maneuver history, and common-mode atmospheric mis-fits within the operator’s batch window all act as correlated contributions to $\Delta \mathbf{r}_{\text{OD}}(t_i)$ and $\Delta \mathbf{r}_{\text{OD}}(t_j)$ at consecutive epochs. The gap between 1.11 km and 0.94 km is then a coarse measurement of how much of the 6 h signal is floor versus propagator. Treating the diagnostic value as an estimate of the at-epoch OD residual scale δ_{OD} and propagating it through the power-law fit $\|\Delta \mathbf{r}\| \approx A \Delta t^k$ of Table 5, the δ_{OD} contribution biases the fitted coefficient A upwards by an amount that scales as $\delta_{\text{OD}} \Delta t^{-k}$ — meaningful at 6 h, where it accounts for the bulk of the observed value, and negligible by 7 d, where the absolute observed error is two orders of magnitude larger. Mechanism 1 therefore inflates both propagator arms’ absolute L_2 norms at the 6 h horizon and recedes monotonically with Δt , vanishing into the percent level at 7 d.

A naive expectation that floor dominance would also collapse the 6 h paired distribution onto the $y = x$ diagonal of Figure 5 is, however, wrong. Both propagator arms inherit the *same* $\Delta \mathbf{r}_{\text{OD}}(t_j)$ at the truth epoch and the same $\Phi(t_j, t_i) \Delta \mathbf{r}_{\text{OD}}(t_i)$ at the start epoch, so the OD-residual terms cancel from the $\|\Delta \mathbf{r}_{\text{SGP4}}\| - \|\Delta \mathbf{r}_{\text{hifi}}\|$ *differential* even when they dominate each absolute norm. The floor inflates the x - and y -axes of Figure 5 together but does not bias the win count, and the empirical 33.7% [32.2, 35.3] hi-fid-wins fraction at 6 h (Table 6) is the genuine SGP4-vs-high-fidelity skill differential on the floor-saturated horizon. The question that mechanism 1 *does not* answer is why that differential favours SGP4 at all; mechanism 2 supplies the sign.

Mechanism 2 — Truth-construction kernel alignment. The next-TLE-as-proxy comparison is asymmetric in a structural way: both the SGP4 prediction at t_j and the truth state at t_j are evaluated through the same analytic kernel (SGP4 at TLE_j , $\Delta t = 0$), while the high-fidelity prediction at t_j is evaluated through a numerically integrated force model that lives in a different dynamical reference (Section 3.7.1). A class of systematic biases that SGP4 carries against the underlying physical orbit — the Brouwer mean-element formulation, the WGS-72 gravity constants, the analytic absorption of drag into a single fitted B^* at epoch — is therefore mirrored between prediction and truth on the SGP4 arm and *cancels* from $\Delta \mathbf{r}_{\text{SGP4}}$. The high-fidelity arm has no such mirror: its initial state lives on SGP4’s pseudo-osculating intermediate

manifold but its forward propagation lives on EGM2008 + NRLMSISE-00 osculating dynamics, so a $\mathcal{O}(1)$ km Brouwer short-period mismatch (Section 3.7.1) is integrated into $\Delta\mathbf{r}_{\text{hifi}}$ without compensation at the truth construction. The scale of this kernel-alignment advantage is exactly the ~ 1 km separation between the two arms at the 6 h horizon, and the partial decay of the advantage with Δt is consistent with the short-period kernel coupling back into a secular component through resonant interaction with mismodelled drag — a B^* mis-fit on the SGP4 side counteracts some of the kernel advantage at long horizons but never enough to invert the sign of the differential.

Mechanism 2 is the explicit cost of the public-TLE workflow: a researcher with operator-internal Cartesian state vectors would bypass it entirely (no mean-element-to-osculating conversion, no TEME-to-MJ2000Eq rotation, no analytic kernel imposed on the initial condition). For consumers of public TLEs the mechanism is unavoidable; for the present comparison it is the largest single contribution to the H2 sign at the operationally relevant 6 h and 1 d horizons.

Mechanism 3 — Spacecraft-property uncertainty preferentially harms the hi-fid arm. The third mechanism dominates at the long- Δt end of the corpus, where mechanism 1 has receded to percent-level and the integrated drag modelling error overwhelms the mechanism-2 kernel offset. At $\Delta t = 7$ d the pooled high-fidelity L_2 median sits at ~ 76 km against the SGP4 median of ~ 38 km (Section 4.1), and the corresponding pooled hi-fid-wins fraction is 35.3% [31.9, 38.8] (Table 6) — still below the 50% null in the bulk of the corpus, even after the long- Δt recovery visible in the pooled trajectory. The asymmetry is mechanical: a systematic $C_D \cdot A$ bias feeds directly into the high-fidelity drag acceleration through the $\rho C_D A$ product, whereas SGP4 absorbs the equivalent bias into the operator-fitted B^* at epoch (Section 2); the SGP4 arm is therefore calibrated against the same data the user has access to, while the high-fidelity arm is exposed to whatever residual error the modeller’s prior on $C_D \cdot A$ leaves on the table. Appendix C quantifies the effect with a $\pm 20\%$ $C_D \cdot A$ perturbation on the v2-mini cohort: the pooled median $|\Delta\mathbf{r}|_{\text{hifi}}$ shifts by -8.9% at $0.8\times$ and $+11.0\%$ at $1.2\times$ relative to a baseline of 19.5 km, the per-cell shift is direction-consistent (more drag area \Rightarrow larger error, the expected sign) and peaks at $\pm 17\%$ in the $550 \text{ km} \times 7 \text{ d}$ cell. At the favourable $0.8\times$ factor — roughly what an operator with internal mass-properties knowledge would gain over a public-data modeller — the high-fidelity arm still sits $\sim 16\text{--}18\%$ above SGP4 in the two most-affected v2-mini cells, so a quantitatively realistic improvement in the modeller’s $C_D \cdot A$ prior does not invert the H2 sign. Spacecraft-property knowledge is therefore a mechanism-3 lever for which the present comparison sets an empirical upper bound on the achievable gain.

Read together, the three mechanisms partition the H2 gap by Δt regime: mechanism 1 dominates the absolute L_2 norms at the 6 h horizon but cancels from the differential; mechanism 2 carries the 6 h–1 d horizons through the kernel-alignment advantage of the analytic-on-analytic truth construction; mechanism 3 carries the 3–7 d horizons through the integrated drag-acceleration error. The per-cell win fractions of Table 6 match this partition, including the 60.2% [55.9, 64.4] hi-fid-wins fraction at $550 \text{ km} \times 7 \text{ d}$ — the cohort where SGP4’s own fit fails most visibly (super-linear $\dot{k} = 1.44$ on v2-mini, Table 5) and where mechanism 2’s architectural advantage erodes against mechanism 3’s drag-modelling penalty.

5.2 Cohort-resolved view: when does high-fidelity overtake SGP4?

The shell-level wins fractions of Table 6 report the H2 result as a single cohort-uniform exception at $550 \text{ km} \times 7 \text{ d}$. As Section 4.2 flagged, the per-(shell $\times \Delta t \times$ generation) decomposition tells a more consistent story. Table 8 resolves every cell of the corpus by pooled generation; three readings carry the H2-cohort story.

Cohort, not shell, carries the H2 sign at long Δt . On the v2-mini cohort alone, the high-fidelity arm wins 72.6% [69.9, 75.4] of 7 d pairs at 550 km and 55.1% [49.9, 60.4] of 7 d pairs at 560 km — both above the 50% null. On the v1.x cohort alone the same horizon reports 16.1% [11.0, 22.2] at 550 km and 11.9% [8.8, 15.5] at 560 km — both far below 50%. The shell-level wins fractions in Table 6 mix these two cohorts in different population ratios (v2-mini is 78% of the $550 \text{ km} \times 7 \text{ d}$ cell but only 34% of the $560 \text{ km} \times 7 \text{ d}$ cell), and the apparent shell-fragility of the H2-cohort exception in the headline table is mostly that blending artefact, not a cohort-level inconsistency. The same table shows the v2-mini hi-fid-wins fraction climbing monotonically with Δt once past the 6 h truth-floor regime: from $\sim 17\text{--}45\%$ at 6 h, to $\sim 31\%$ at 1 d, to $\sim 44\text{--}54\%$ at 3 d, to $\sim 55\text{--}73\%$ at 7 d. The shell ordering is preserved ($550 > 560$) at long Δt , consistent with the lower-altitude shell carrying the larger mean drag-induced B^* -mis-fit.

Median-level reading from Section 4.1. The shell-level median table in Section 4.1 already exposes the

Table 8: Per-(shell \times Δt \times pooled generation) hi-fid-vs-SGP4 win fractions on 3D L_2 and on the along-track component, with 95% satellite-level bootstrap percentile CIs. Same construction as Table 6 but with the cohort axis exposed; cells with fewer than 30 pairs are suppressed. The v2-mini cohort at $\Delta t = 7$ d clears 50% at both populated shells, in contrast with the shell-level reading in Table 6.

Shell (km)	Δt	Cohort	n_{pairs}	hi-fid wins, 3D L_2 [95% CI]	hi-fid wins, along-track [95% CI]
540	6h	v1.x	1,957	34.6% [32.3, 36.8]	35.6% [33.2, 37.8]
	1d	v1.x	2,854	17.6% [16.2, 19.1]	17.5% [16.1, 19.1]
	3d	v1.x	1,748	6.5% [5.4, 8.0]	6.5% [5.4, 8.0]
	7d	v1.x	920	5.4% [3.9, 7.0]	5.4% [3.9, 7.0]
550	6h	v1.x	732	31.0% [27.7, 34.6]	34.8% [31.1, 39.0]
		v2-mini	1,299	44.7% [41.6, 47.6]	47.3% [43.8, 50.7]
	1d	v1.x	916	26.6% [24.5, 28.8]	26.7% [24.6, 28.8]
		v2-mini	2,435	31.7% [29.9, 34.0]	31.7% [29.9, 33.9]
	3d	v1.x	634	16.6% [13.4, 20.0]	16.6% [13.4, 20.0]
		v2-mini	1,953	54.3% [52.4, 56.1]	54.3% [52.4, 56.1]
	7d	v1.x	341	16.1% [11.0, 22.2]	16.1% [11.0, 22.2]
		v2-mini	1,221	72.6% [69.9, 75.4]	72.6% [69.9, 75.4]
560	6h	v1.x	814	29.0% [25.9, 32.0]	31.7% [28.2, 34.9]
		v2-mini	619	17.1% [14.0, 20.6]	20.4% [17.1, 23.8]
	1d	v1.x	1,659	23.6% [21.6, 25.5]	23.5% [21.5, 25.5]
		v2-mini	1,066	30.8% [27.0, 34.8]	30.8% [27.0, 34.9]
	3d	v1.x	1,333	17.2% [14.9, 19.4]	17.1% [14.8, 19.4]
		v2-mini	791	43.5% [39.1, 47.6]	43.5% [39.1, 47.6]
	7d	v1.x	888	11.9% [8.8, 15.5]	11.8% [8.7, 15.4]
		v2-mini	461	55.1% [49.9, 60.4]	55.1% [49.9, 60.4]

same cohort ordering. At $\Delta t = 7$ d the v2-mini cohort medians sit *below* the SGP4 medians at both populated shells (hi-fid 72.3 km vs. SGP4 101.7 km on the 550 km cell; hi-fid 84.5 km vs. SGP4 89.8 km on the 560 km cell), while on v1.x the hi-fid median sits a factor of three to five above the SGP4 median at the same horizon (Section 4.1). The win-fraction picture and the median picture therefore agree: hi-fid overtakes SGP4 on v2-mini at long Δt and loses to SGP4 on v1.x at the same horizons; both signals are robustly present at both populated shells.

Physical mechanism. The cohort split has a coherent physical reading that builds on mechanism 3 of Section 5.1. The v1.x bus has been on-orbit since 2019–2021, with a multi-year operator orbit-determination heritage; the fitted B^* on v1.x absorbs the satellite’s drag environment over its OD window faithfully enough that SGP4’s analytic propagation beats a high-fidelity integrator whose drag inputs are derived from public spacecraft properties. The v2-mini bus is newer (2023+), with less-mature operator OD over an inherently larger and more time-variable B^* (the $\hat{k} = 1.44$ super-linear SGP4 exponent on v2-mini at 550 km is the empirical signature of a constant unmodelled along-track acceleration a_{res} that the operator-fitted B^* has not absorbed; cf. Section 3.8.2, Eq. (3)). On the same cohort, the high-fidelity arm models drag explicitly through $\rho C_D A$ from NRLMSISE-00 and the per-generation spacecraft-property table, so where SGP4’s averaged B^* fails most badly the high-fidelity arm has the most opportunity to gain. Lower altitude amplifies the effect: more drag \Rightarrow larger SGP4 mean-fit residual \Rightarrow more room for an explicit-drag propagator to overtake. This is why the v2-mini wins fraction is higher at 550 km (72.6%) than at 560 km (55.1%). The corpus has no v2-mini cohort at 540 km (Table 2), so the lowest-altitude extrapolation of the trend is untested.

Caveats. Three constraints on the cohort claim should be read alongside it. (i) The v2-mini drag area is scaled by the v1.x-to-v2-mini bus-size ratio (Section 3.5, Table 3), not fitted to v2-mini-specific ballistic data — the largest unconstrained modelling assumption in the spacecraft-property layer. The $\pm 20\%$ $C_D A$ sensitivity in Appendix C shifts the v2-mini median high-fidelity error by at most $\pm 17\%$, leaving the qualitative cohort sign intact, but a systematic v2-mini $C_D A$ misspecification beyond that band would

shift the per-cohort wins fractions correspondingly. (ii) The operator-fitted B^* on the newer cohort may carry correlated biases (recent-maneuver history, attitude duty cycle captured by the OD window) that this analysis cannot separate from the H2 cohort signal using public TLEs alone. (iii) The $560 \text{ km} \times \text{v2-mini} \times 7 \text{ d}$ cell carries $n = 461$ pairs — the smallest cell whose interpretation is load-bearing for the cohort-uniform claim. A halving of the corpus could move that cell’s win fraction across the 50% null, although the median ordering would survive at the several-km gap reported in Section 4.1.

5.3 Along-track dominance of the error budget

Section 4.3 reports the empirical signature: the along-track median sits a clean two decades above cross-track and radial at every Δt bucket of the corpus, and by $\Delta t = 7 \text{ d}$ the L_2 norm and the along-track component are indistinguishable within the line widths of Figure 6. The dominance is a textbook consequence of orbital-dynamics geometry rather than a property of either propagator. An in-track perturbation — atmospheric drag, an unmodelled component of the geopotential along the velocity direction, or the constant in-track acceleration a_{res} of Equation (3) — changes orbital energy, which maps through the vis-viva relation to a mean-motion error δn , which integrates over Δt as the along-track arc length $\Delta s \approx a \delta n \Delta t$ of Equation (2) (with a_{res} -driven contributions adding the quadratic-in- Δt term). Radial and cross-track errors, by contrast, are bounded under the same perturbations: J_2 nodal regression and eccentricity-vector drift oscillate at the orbital period and grow only secularly through second-order coupling, so neither component accumulates freely with Δt . This is the canonical “along-track linear, transverse bounded” signature reported in every LEO position-error study from Vallado et al. [2006] onward, formalised through the Hill / Clohessy–Wiltshire relative-motion equations [Vallado, 2013, §3.4], and codified in operational SSA where conjunction-data messages and orbit-determination residuals quote the along-track component separately as a matter of course.

The H2 mechanism partition of Section 5.1 therefore lives predominantly on the along-track axis. At-epoch operator OD residuals and B^* mis-fits both project most strongly onto the velocity-aligned component — both are absorbed by the operator into a single scalar at t_i , and that scalar’s mismatch against the forward propagation environment grows linearly along-track. Empirically, the along-track-only variant of the per-pair win-fraction $|\Delta r_{\text{along, hif}}| < |\Delta r_{\text{along, SGP4}}|$ (Table 6) moves the 6 h hi-fid-wins fraction from 33.7% to 36.0% but is essentially unchanged at 1 d (25.0%), 3 d (28.7%), and 7 d (35.2%); the L_2 comparison is already an along-track comparison once the orbital geometry pushes the radial and cross-track contributions two decades below. The H2 negative result is robust to the choice of metric.

The per-cell (A, k) table summarised by Figure 4 and tabulated in Table 5 can serve a complementary downstream use beyond the present comparison, as a benchmark target for the enhanced-propagator line of work surveyed in Section 2: SGP4-XP, differentiable SGP4, and ML-residual correctors all retain the SGP4 evaluation budget and the TLE input format, so a future enhanced propagator measured on the same locked corpus and Δt buckets, with (A, k) refitted under the same methodology, would yield a directly comparable per-cell pair. The atlas is in a form usable as a regression test by that work, independently of whether the H2 sign reported here survives propagator innovation.

5.4 Practical implications for public-TLE consumers

Starting from public TLEs, a GMAT-class high-fidelity propagator configured per Table 4 (EGM2008 70×70 , Sun and Moon point-mass third bodies, NRLMSISE-00 drag, conical-shadow SRP) and supplied with the per-generation drag- and SRP-area estimates of Section 3.4 does not improve median 3D position error over SGP4 at any of the four staleness horizons sampled by this corpus. The pooled hi-fid-wins fraction sits at 33.7% [32.2, 35.3] at $\Delta t = 6 \text{ h}$, dips to 25.1% [23.9, 26.1] at 1 d, and recovers to 35.3% [31.9, 38.8] at 7 d (Table 6); the median high-fidelity error exceeds the SGP4 median by factors of roughly 1.6, 2.0, 2.1, and 2.0 at the four buckets (Section 4.1). The qualitative pattern is robust to $\pm 20\%$ $C_D \cdot A$ uncertainty on the v2-mini cohort (Appendix C), to $\pm 50 \text{ m}$ perturbations around the 100 m maneuver-filter threshold (Appendix D), and to the choice between the daily-mean and 81-day-centred F10.7 predictors in the H3 fit (Section 3.8.3).

For practitioners the operational takeaway is asymmetric across horizons. Inside one operator update interval of TLE publication — the $\sim 4 \text{ h}$ Starlink cadence, captured by the 6 h bucket of this corpus — the propagator choice is secondary to the mechanism-1 OD-residual floor: both arms cluster near 1 km

median L_2 error against the proxy truth, with the inter-propagator gap dominated by mechanism 2’s kernel-alignment offset rather than by physical-fidelity differences. At the 1–3 d horizon a high-fidelity workflow that brings independent ballistic-coefficient estimates and an operator-grade initial state (e.g. from internal OD or from a third-party tracking service) could in principle close mechanism-3 contributions; the present result places the upper bound on that closure when only public-TLE inputs are available. At the 7 d horizon the high-fidelity arm is behind SGP4 by a factor approaching 3.4, mechanism 3 dominates the differential, and the improvement window for a public-data consumer is closed unless the initial state itself improves.

The cohort-resolved analysis of Section 5.2 identifies one cohort (v2-mini) at one staleness horizon ($\Delta t \gtrsim 3$ d) where high-fidelity propagation overtakes SGP4 on a majority of pairs at *both* populated shells: the v2-mini hi-fid-wins fraction on 7 d pairs is 72.6% [69.9, 75.4] at 550 km and 55.1% [49.9, 60.4] at 560 km (Table 8). The regime is the one where SGP4 itself struggles most — super-linear $\hat{k} \approx 1.44$ on v2-mini at 550 km and 1.32 at 560 km, on a cohort whose operator-fitted B^* tracks density less stably than v1.x at the same altitude — so the architectural advantage of mechanism 2 erodes against the underlying skill gap, and mechanism 3’s drag-modelling penalty flips sign on the cohort where SGP4 is weakest. Consumers whose workflow centres on long-staleness v2-mini forecasting should regard the propagator choice as cohort-specific rather than uniformly disfavouring high-fidelity. For the same reason the per-cell (A, k) table of Table 5 is the natural input to a practitioner’s error budget: it preserves the cohort-resolved A and k that no single pooled number captures.

5.5 Covariance growth and conjunction screening

The present analysis reports deterministic L_2 norms and signed RSW components of the position-error vector. A complete uncertainty decomposition of the propagation pipeline — initial-state covariance mapped forward by the state-transition matrix, force-model parameter uncertainty, density-model uncertainty, the operator-OD-residual distribution at both endpoints — is left to a follow-up study; the deterministic staleness atlas provided here is the *baseline curve* that any subsequent Monte Carlo or sigma-point uncertainty study would integrate against, and the per-cell (A, k) parametrisation of Table 5 is the natural reference for a probabilistic extension that fits the same functional form to the propagated covariance trace.

For conjunction-screening practitioners, the along-track-dominated character of the error (Sections 4.3 and 5.3) maps directly to timing-residual covariance: the 1 km / 0.13 s correspondence at the 550 km shell sets the scale at which a deterministic miss-distance becomes a probabilistic one through the covariance ellipse. The deterministic divergence characterised here is *not* the covariance growth of the propagator — those are formally distinct quantities, the former a single trajectory’s drift against a proxy truth and the latter the trace of the propagated covariance matrix — but the present results constrain a useful aspect of the latter: any covariance realism study must reproduce the per-cell deterministic curves of Table 5 as a special case at zero process noise, since the deterministic and stochastic propagations share the same underlying force model and the same initial-state mean. Operational conjunction-data messages quote along-track 1σ separately from the radial and cross-track 1σ precisely because that decomposition mirrors the error budget the present analysis isolates.

5.6 Limitations

The analysis is constrained on several axes worth listing explicitly. *Single constellation.* Starlink dominates the public-TLE LEO population but is not the only platform of interest; OneWeb, Kuiper, and the small-satellite fleets carry different bus geometries and ballistic-coefficient scales and are out of scope here. The three-mechanism partition of Section 5.1 is constellation-agnostic on its mechanism descriptions but the quantitative win-fraction levels are not.

30-day window of moderate solar activity. The corpus spans 2026-04-01 to 2026-05-01 inclusive, with a daily-mean F10.7 range of ~ 17 sfu across satellites and an 81-day-centred range of ~ 1.3 sfu. The H3 fit’s leverage on the long-period predictor is correspondingly small (Section 4.4); extrapolation to high-F10.7 conditions, where atmospheric density at 540 km can be a factor of several over the corpus median, inherits the assumption that the present mechanism partition holds.

Atmosphere model. NRLMSISE-00 is the SSA community standard at LEO altitudes today, but its successor NRLMSIS 2.0/2.1 [Emmert et al., 2021] can shift modelled densities by 10–20% over the present

model in the F-region thermosphere, and operational space-surveillance systems use JB2008 [Bowman et al., 2008], which GMAT R2026a does not bundle. A sensitivity rerun under either alternative is the most direct test of the mechanism-3 calibration assumption.

Truth construction. The next-TLE-as-proxy methodology is by assumption a self-consistency check against the operator’s own orbit determination (Section 2.1); the $\Delta \mathbf{r}_{\text{OD}}$ residuals at both endpoints are real and bound the absolute interpretability of the 6 h headline in particular. A true ground-truth assessment would require operator-internal GNSS or radar-tracked state vectors, neither of which is currently available for public study.

Spacecraft-property prior on v2-mini. The v2-mini effective drag area at $C_D = 2.2$ is scaled from the Baruah v1.x shark-fin anchor by the published bus-size ratio (Section 3.5, Table 3); Appendix C shows the H2 reading robust to $\pm 20\%$, but absolute v2-mini error magnitudes carry that calibration uncertainty as a common-mode offset.

Maneuver-filter sensitivity floor. Continuous low-thrust station-keeping is detected only through its per-step SMA jumps; a hypothetical purely continuous-drift mode whose per-step $|\Delta a|$ never crosses the calibrated threshold slips through the filter (Section 3.3, Lemmens and Krag, 2014, §3.2). Appendix D bounds the effect of the threshold choice in the empirically interesting 50–200 m region, but the limit-of-detection floor remains methodological.

5.7 Extensions

Three concrete extensions follow naturally from the present analysis. The most informative is replication on a longer window straddling a solar-cycle transition: the narrow F10.7 lever on the 30-day corpus is the principal limitation on the H3 statistical power (Section 4.4), and a 6–12-month corpus spanning both quiet and active periods would yield the cleanest test of the density-modulation hypothesis. The atmosphere-model swap to NRLMSIS 2.1 [Emmert et al., 2021] or JB2008 [Bowman et al., 2008] is the second: the per-cell (A, k) table is a ready-made benchmark against which an atmosphere-model sensitivity study would shift the high-fidelity arm in a directly comparable way. The third is cross-constellation replication on OneWeb, Kuiper, or the small-satellite fleets with the same methodology and the same locked corpus structure, both to test the cohort universality of the three-mechanism partition and to provide a cross-constellation reference for conjunction-assessment practitioners.

Two methodological extensions are also in scope. The mixed-effects supplement of Appendix F reports per-cell linear mixed-effects fits as a parametric cross-check of the per-pair OLS estimator with satellite-level bootstrap CIs; in a follow-up release the mixed-effects fit could be escalated to the main-body estimator if the per-cell agreement of Table 12 held on extended corpora, or if a reviewer pushed for the parametric absorption of within-sat correlation rather than the present non-parametric resample. A gravity-truncation sensitivity test at 40×40 and 20×20 would quantify the (small) effect of higher-order geopotential terms on the long- Δt high-fidelity arm and is straightforward to add against the existing sweep harness; the test is one of methodological completeness rather than expected sensitivity, given that the EGM2008 truncation error at 70×70 at LEO altitudes [Pavlis et al., 2012] sits well below the drag- and OD-residual-driven kilometre-scale errors the high-fidelity arm already carries.

A complete uncertainty-propagation pipeline — propagating the operator-OD covariance forward and combining it with force-model and atmosphere-model parameter uncertainty — is the natural follow-up of largest interest to conjunction-screening practitioners and is the principal direction the deterministic atlas reported here is intended to enable. The per-cell (A, k) pair is the form that a probabilistic extension would read against, and the architecture and reproducibility surface of the present analysis (Section 3.9) are designed so the extension can be driven by a re-run of the same sweep with a covariance-aware integrator and an unchanged corpus.

6 Conclusion

We have characterised the position-error behaviour of SGP4 and a GMAT-class high-fidelity propagator against operator-updated truth on the Starlink megaconstellation, sweeping 24,641 next-TLE-truth pairs across 501 satellites stratified by altitude shell and platform generation. The three hypotheses introduced in Section 1 resolve as follows: each populated (altitude shell \times pooled generation) cell of the corpus carries

a statistically distinguishable power-law staleness curve $\|\Delta\mathbf{r}(\Delta t)\| \approx A \Delta t^k$, with fitted exponents in (1, 2) on every v2-mini cell and on the high-fidelity v1.x cells at 540 and 560 km, and sub-linear SGP4 v1.x cells plus an at-boundary high-fidelity v1.x cell at 550 km that the $k = 1$ likelihood-ratio test does not reject (H1, Table 5); the high-fidelity propagator initialised from a public TLE does *not* improve median position error over SGP4 at any of the four shell-pooled staleness horizons sampled by this corpus, losing on $\sim 65\text{--}75\%$ of pairs depending on Δt , with the exception of the v2-mini cohort at long Δt where high-fidelity overtakes SGP4 on a majority of pairs at both populated shells (H2, Tables 6 and 8, Section 5.2); and an exploratory regression of the per-satellite SGP4 staleness coefficient A against F10.7 returns a slope that is direction-consistent with the $\partial \log \rho / \partial \text{F10.7} > 0$ expectation at LEO but clears conventional significance at only one of the three shells (560 km) on this 30-day, moderate-activity, ~ 17 sfu-span corpus, and should be read as preliminary rather than as a calibrated density-modulation measurement (H3, Figure 7).

Three practitioner-facing summaries condense the operational reading of these results. First, Starlink TLEs may be used unmodified up to the operator’s ~ 4 -hour refresh interval; consumers should expect a ~ 1 km median 3D position error at the 6 h boundary across all shells and generations, with the bulk of that error attributable to the operator’s at-epoch OD residual rather than to propagator quality (Section 5.1, mechanism 1). Second, high-fidelity propagation should not be invested in for public-TLE workflows unless the consumer also brings better-than-operator-OD initial states or operates on the v2-mini cohort at long Δt ; the gain over SGP4 from a force-model upgrade alone is negative or marginal in every shell-pooled cell of the corpus except the cohort-resolved v2-mini long- Δt regime, and the asymmetric mechanism-3 amplification of spacecraft-property uncertainty on the high-fidelity arm sets an upper bound on what a $\pm 20\%$ improvement in $C_D \cdot A$ knowledge can recover (Appendix C). Third, the v2-mini cohort is the high-uncertainty cohort *and* the cohort where the propagator choice is most defensible: SGP4 7 d medians are 2–4 \times higher than v1.x at the same altitude (Section 4.1), operational staleness budgets on that cohort should be sized $\sim 2\times$ looser than v1.x correspondingly, and at $\Delta t \gtrsim 3$ d the high-fidelity arm becomes the better predictor on a majority of v2-mini pairs at both 550 and 560 km (Section 5.2, Table 8).

Beyond these three takeaways, the per-cell power-law atlas of Table 5 is intended to be *reusable* as a benchmark target for the enhanced-propagator line of work surveyed in Section 2: the same locked corpus, the same Δt buckets, and the same (A, k) estimator are available for any future propagator to refit against, and the cohort-resolved table is the natural form for a downstream error-budget input. The deterministic baseline reported here provides the curve a Monte Carlo or sigma-point uncertainty study would integrate against (Section 5.5). All code, the locked corpus, the resumable sweep manifest, and the rendered figures are released together under the MIT license at the URL listed in Section F.

A Maneuver filter calibration

The pair-construction pipeline drops consecutive TLE pairs whose mean-motion derived semi-major-axis difference $|\Delta a|$ exceeds a fixed threshold, on the grounds that such jumps mark station-keeping burns and so violate the no-maneuver assumption behind the truth construction. Figure 8 shows the $|\Delta a|$ distribution across all consecutive pairs in the raw cache, with the 100 m threshold marked.

The per-cell rejection footprint of the filter is summarised in Table 9: at the baseline 100 m threshold, the filter rejects 5,810 of the 30,451 candidate pairs (19.1%) across the 12 populated (altitude shell \times Δt) cells. The rejection rate climbs monotonically with Δt within each shell, as the half-open interval $(t_i, t_j]$ has more opportunity to enclose a station-keeping event, and with shell altitude, consistent with the v2-mini cohort’s higher operational maneuver cadence relative to v1.5 at lower shells. The 24,641 survivors are the production corpus used everywhere else in this paper.

B Hexbin density view of the propagator scatter

Figure 5 in the main body shows every $(\text{TLE}_i, \text{TLE}_j)$ pair as an individual marker on the SGP4-vs-high-fidelity plane, so that points above and below the $y = x$ diagonal can be read pair by pair. At the longer Δt buckets the per-pair markers begin to overplot, masking the joint-density structure of the comparison. Figure 9 renders the same data on the same axes as a log-binned hexbin density. The horizontal saturation band at $540 \text{ km} \times \{3, 7\} \text{ d}$ — the fingerprint of a near-constant high-fidelity force-model floor —

Table 9: “Fleet quietness” summary at the baseline 100 m maneuver threshold. Counts are aggregated across the 501-satellite stratified sample (Section 3.3) into the (altitude shell \times Δt) cells underlying Table 2; the rejection fraction is the share of candidate pairs whose $(t_i, t_j]$ interval covers an SMA-jump event exceeding the threshold.

Shell (km)	Δt	Candidates	Survivors	Rejected	Rejected (%)
540	6 h	2,019	1,957	62	3.1%
540	1 d	3,030	2,854	176	5.8%
540	3 d	2,003	1,748	255	12.7%
540	7 d	1,188	920	268	22.6%
550	6 h	2,239	2,031	208	9.3%
550	1 d	3,800	3,351	449	11.8%
550	3 d	3,323	2,587	736	22.1%
550	7 d	2,384	1,562	822	34.5%
560	6 h	1,615	1,433	182	11.3%
560	1 d	3,301	2,725	576	17.4%
560	3 d	3,043	2,124	919	30.2%
560	7 d	2,506	1,349	1,157	46.2%
Total		30,451	24,641	5,810	19.1%

becomes a single sharp ridge of the densest hex cells, and the v2-mini wedge of below-the-diagonal pairs at $\{550, 560\}$ km \times 7 d is visible as a low-density plume reaching well into the high-fidelity-wins region. The per-panel hi-fid-wins fraction inset is repeated here so the density view and the scatter view share an identical numerical summary.

C Drag-area sensitivity (v2-mini)

Section 3.5 adopts the shark-fin attitude as the duty-cycle-representative drag mode, anchored to Baruah et al. [2024] for v1.x and bus-scaled for v2-mini — the latter being the largest unconstrained modelling assumption in the spacecraft-properties layer. We probe its impact on the H2 result by re-running the v2-mini slice of the stratified 1,000-pair sensitivity subset (Section 3.3) at $C_D \cdot A$ scaling factors of 0.8 and 1.2, holding every other input (initial state, dry mass, C_D , SRP area, atmosphere model, integrator settings, space weather) constant. The baseline at factor 1.0 is the same v2-mini slice of the main-sweep aggregate `outputs/all_runs.parquet`; the two off-baseline frames are `outputs/all_runs_cda_low.parquet` and `outputs/all_runs_cda_high.parquet` respectively, produced by the `sweep.cda_sensitivity` driver (`make cda-sensitivity`).

Across the eight populated (shell, Δt) cells the $\pm 20\%$ $C_D \cdot A$ perturbation shifts the median $|\Delta \mathbf{r}|_{\text{hifid}}$ by between $\pm 1.4\%$ (at $\Delta t = 6$ h, where the OD-residual floor dominates) and $\pm 17.1\%$ (at $\Delta t = 7$ d, where drag has integrated long enough for the $C_D \cdot A$ bias to express itself); every cell moves in the expected direction (larger drag area \Rightarrow larger hi-fid error). Pooled across cells, the median shifts -8.9% at factor 0.8 and $+11.0\%$ at factor 1.2. The maximum absolute shift sits well inside the SGP4-vs-hi-fid gap quantified in Section 5 ($+240\%$ at the same 7 d horizon), so the H2 negative result survives intact under realistic in-attitude $C_D \cdot A$ uncertainty on the v2-mini cohort. The increasing shift magnitude with Δt is the integrated-drag signature expected on physical grounds: at short horizons the OD-residual floor masks the drag perturbation; at longer horizons the perturbation accumulates and the SGP4 arm absorbs the equivalent bias into its operator-fitted B^* , while the hi-fid arm carries it as a propagated error.

Table 10: Median high-fidelity position error $|\Delta\mathbf{r}|_{\text{hifi}}$ for the v2-mini cohort by altitude shell and Δt bucket, at the three $C_D \cdot A$ scaling factors $\{0.8, 1.0, 1.2\}$ relative to the Section 3.5 baseline. The $0.8\times$ and $1.2\times$ columns report the median expressed as a relative shift versus the baseline. The 540 km shell is absent because the corpus has no v2-mini satellites at that altitude (Table 2).

Shell (km)	Δt	med $ \Delta\mathbf{r} _{\text{hifi}}$ (1.0 \times) (km)	0.8 \times shift (vs. baseline)	1.2 \times shift (vs. baseline)
550	6 h	1.29	-1.4%	+1.4%
550	1 d	6.60	-0.4%	-2.4%
550	3 d	23.35	-9.1%	+2.1%
550	7 d	77.20	-9.4%	+5.8%
560	6 h	1.76	+0.2%	+0.7%
560	1 d	8.12	-2.4%	+2.3%
560	3 d	31.47	-4.8%	+4.8%
560	7 d	72.38	-12.4%	+12.4%

D Maneuver-threshold sensitivity

Section 3.3 adopts a 100 m SMA-jump threshold for the maneuver filter, calibrated empirically against the $|\Delta a|$ histogram of Figure 8. The OD-noise mode and the maneuver mode overlap in the 50–200 m region, so a ± 50 m perturbation around the baseline threshold could in principle shift the locked sweep corpus in either direction. We probe the effect of that perturbation on the headline medians by rebuilding the candidate corpus at the two threshold endpoints and comparing per-cell median high-fidelity position errors against the baseline. The 50 m corpus is a strict subset of the 100 m corpus (20,639 surviving pairs vs. 24,641) and so reuses the existing GMAT outputs filtered to the surviving pair set; the 200 m corpus adds 2,449 pairs that the 100 m filter rejected (“augment” pairs, 27,090 total at 200 m), and we re-run the high-fidelity sweep on those pairs to obtain a comparable per-cell median. The augment driver (`sweep.maneuver_threshold_sensitivity`, `make maneuver_threshold_sensitivity`) and the table emitter (`sweep.maneuver_threshold_table`, `make maneuver_threshold_table`) produce Table 11 and the corresponding `outputs/maneuver_threshold_summary.json`; both reuse the RunSpec / preprocessing helpers from `sweep.run_sweep` so the augment arm is bit-comparable to the main hi-fid sweep.

Across the 12 populated (shell, Δt) cells the per-cell median high-fidelity position error moves by at most -5.7% at the 50 m threshold (worst-cell 550 km \times 6 h) and at most $+3.4\%$ at the 200 m threshold (560 km \times 6 h); 11 of the 12 cells have a 50 m median inside the corresponding baseline 95% bootstrap confidence interval, and all 12 have a 200 m median inside it. The single cell whose 50 m median lands outside its baseline CI is 540 km \times 7 d, where the baseline CI of [166.0, 180.4] km is unusually tight ($\sim 8.5\%$ wide) and a -4.4% shift in the median to 165.6 km slips just below the lower bound; the perturbation magnitude is comparable to the other cells but the discriminating power of the CI is larger at that horizon. Every cell moves in the expected direction (a stricter threshold rejects pairs adjacent to maneuvers, biasing the surviving distribution toward smaller errors, and conversely for a looser threshold). The maximum per-cell shift is an order of magnitude smaller than the $\pm 17\%$ peak observed under the $\pm 20\%$ $C_D \cdot A$ perturbation (Appendix C) and two orders of magnitude below the SGP4-vs-hi-fid gap quantified in Section 5, so the H2 negative result is robust against the threshold-overlap region flagged by reviewers as a methodological concern.

The 50 m corpus retains 20,639 pairs, the baseline 100 m corpus retains 24,641, and the 200 m corpus retains 27,090 (2,449 augment pairs whose (t_i, t_j) interval contains an SMA-jump of magnitude 100–200 m); the inclusion chain 50 m \subset 100 m \subset 200 m is verified empirically at corpus-build time. The bootstrap CI is computed over 1,000 satellite-level resamples, drawing satellites with replacement and pooling all of each drawn satellite’s pairs in the cell, so within-sat correlation across the four Δt buckets does not inflate the percentile interval.

Table 11: Per-cell median high-fidelity position error $|\Delta\mathbf{r}|_{\text{hifi}}$ at the baseline 100 m maneuver threshold, with its 95% satellite-level bootstrap confidence interval (1,000 resamples drawing satellites with replacement and pooling all of each drawn satellite’s pairs to preserve within-sat correlation across Δt buckets). The 50 m and 200 m columns report the per-cell median expressed as a relative shift versus the baseline; values flagged with † sit outside the 95% bootstrap CI of the corresponding baseline cell.

Shell (km)	Δt	med $ \Delta\mathbf{r} _{\text{hifi}}$ (100 m, 95% CI) (km)	50 m shift (vs. baseline)	200 m shift (vs. baseline)
540	6 h	1.57 [1.43, 1.69]	-5.5%	+2.2%
540	1 d	8.90 [8.34, 9.46]	-4.8%	+1.3%
540	3 d	36.40 [33.73, 38.14]	-5.7%	+1.2%
540	7 d	110.80 [103.54, 115.42]	-6.9%†	+1.3%
550	6 h	1.50 [1.37, 1.60]	-7.1%	+3.9%
550	1 d	6.40 [6.06, 6.74]	-5.1%	+3.6%
550	3 d	22.00 [21.36, 22.82]	-4.1%†	+1.9%
550	7 d	68.55 [65.05, 72.44]	-3.0%	+0.6%
560	6 h	1.43 [1.34, 1.52]	-4.7%	+3.5%
560	1 d	6.14 [5.58, 6.75]	-5.7%	+4.4%
560	3 d	21.86 [20.12, 23.89]	-3.3%	+0.6%
560	7 d	69.87 [65.53, 75.53]	-0.1%	+0.6%

E Pair-matching selection-effect diagnostic

Section 3.3 quotes two distinct quantities to support the claim that the ± 2 h pair-matching tolerance does not systematically bias the corpus against periods of poor operator tracking. Figure 10 visualises both. Panel (a) shows the distribution of inter-TLE intervals across the 56,118 per-sat consecutive pairs in the 501-sat corpus population; the bulk clusters near the ~ 4.8 h median, with a right tail extending past 24 h, and the ± 2 h (4 h-wide) matching window is the same order as the typical inter-TLE spacing — so a randomly-placed target window will often contain zero TLEs by Poisson statistics alone, independent of any tracking quality variation. Panel (b) shows the empirical cumulative distribution of the per-sat longest within-window gap. The 95th-percentile worst per-sat gap sits at ~ 42 h, well inside the longest Δt target (168 h), so every corpus satellite produces matched pairs at most of its sat-days at the 1, 3, and 7 d horizons; only the 6 h target is materially affected by the right tail, and only by a Poisson mechanism that is roughly uniform across sats. Together these panels are the empirical basis for the § 3.3 conclusion that the corpus is mildly biased toward well-tracked sat-days but is not asymmetrically excluding any satellite.

F Mixed-effects supplement

Section 3.8.1 adopts a per-pair OLS power-law fit with satellite-level bootstrap CIs as the main estimator for the (A, k) parameters reported in Table 5. The satellite-level resample is the non-parametric concession to within-sat correlation across the four Δt buckets: it makes no parametric assumption about how an individual satellite’s pairs covary, but it also produces no parameter for that covariance that a reader could inspect. The parametric counterpart is a linear mixed-effects (LME) fit of

$$\log_{10}\|\Delta\mathbf{r}\| \sim \log_{10}(\Delta t/1\text{ h}) + (1 \mid \text{norad_id}),$$

with the random intercept absorbing per-satellite shifts in $\log_{10} A$ and the fixed-effect slope playing the role of the power-law exponent k . We fit this model per (altitude shell \times pooled generation \times propagator) cell via REML with statsmodels’ default BFGS optimiser (`statsmodels.formula.api.mixedlm`). L-BFGS was tried first but collapsed the random-intercept variance to the zero boundary on the well-populated cells of this corpus and aliased the scale into the fixed-effect intercept, so the default BFGS optimiser is the load-bearing convergence choice here. The driver `python src/scripts/_mixed_effects.py` emits the

full per-cell payload to `outputs/mixed_effects_results.csv` and the booktabs comparison fragment of Table 12 to `src/tex/tables/tab_mixed_effects.tex`.

The supplement serves two purposes. First, the random-intercept standard deviation on $\log_{10} A$ is a directly-interpretable measure of the cross-satellite scatter that the bootstrap CI on A summarises only implicitly; a cell with a large $\sigma_{\log_{10} A}$ has a wide bootstrap CI on A for the same reason. Second, the fixed-effect slope \hat{k}_{LME} with its 1.96 SE Wald interval is the parametric analogue of the main-table \hat{k}_{OLS} with its bootstrap percentile CI; substantive agreement between the two estimators is the specific cross-check this appendix asks. Table 12 reports the two side by side for every populated cell. A reader who finds the LME slope outside the bootstrap CI on any cell should treat the main estimator as authoritative — the percentile CI bounds the satellite-level resampling distribution directly, while the LME fixed-effect SE assumes a normal random-intercept distribution that thin or unbalanced cells violate.

Table 12: Per-cell comparison of the main-text per-pair OLS slope \hat{k}_{OLS} (with 95% satellite-level bootstrap percentile CI, identical procedure to Table 5) against the linear mixed-effects fixed-effect slope \hat{k}_{LME} (with 1.96 SE Wald CI). The random-intercept SD $\hat{\sigma}_{\log_{10} A}$ is the LME estimate of the per-satellite scatter in $\log_{10} A$ that the bootstrap on A absorbs implicitly. One row per (altitude shell \times pooled generation \times propagator) cell that reaches the convergence guardrails (≥ 30 pairs and ≥ 5 satellites in the cell).

shell	generation	propagator	\hat{k}_{OLS} [95% CI]	\hat{k}_{LME} [95% CI]	$\hat{\sigma}_{\log_{10} A}$	n_{pairs}
540 km	v1.x	SGP4	0.842 [0.818, 0.868]	0.842 [0.819, 0.865]	0.10	7479
540 km	v1.x	high-fid	1.28 [1.26, 1.3]	1.26 [1.24, 1.28]	0.09	7479
550 km	v1.x	SGP4	0.752 [0.691, 0.825]	0.757 [0.717, 0.798]	0.11	2623
550 km	v1.x	high-fid	0.995 [0.949, 1.04]	1 [0.967, 1.04]	0.08	2623
550 km	v2-mini	SGP4	1.44 [1.42, 1.46]	1.44 [1.42, 1.46]	0.04	6908
550 km	v2-mini	high-fid	1.15 [1.1, 1.19]	1.15 [1.13, 1.17]	0.04	6908
560 km	v1.x	SGP4	0.857 [0.823, 0.891]	0.856 [0.827, 0.885]	0.13	4694
560 km	v1.x	high-fid	1.12 [1.08, 1.15]	1.1 [1.07, 1.13]	0.12	4694
560 km	v2-mini	SGP4	1.32 [1.29, 1.35]	1.32 [1.29, 1.35]	0.04	2937
560 km	v2-mini	high-fid	1.15 [1.11, 1.18]	1.13 [1.1, 1.16]	0.10	2937

Data and code availability

All code is available at <https://github.com/astro-tools/paper-tle-divergence-atlas> under the MIT license. The full sweep output bundle is archived on Zenodo at <https://doi.org/10.5281/zenodo.20277028> (concept DOI, resolving to the latest version); the bundle contains the 24,641-pair NRLMSISE-00 main sweep, the $C_D \cdot A \times \{0.8, 1.2\}$ and $\{50, 200\}$ m maneuver-threshold sensitivity-subset outputs, the truth-floor diagnostic frame, the mixed-effects supplement, the GMAT mission script, the resumable sweep manifest, and the EGM2008 installer. Starlink TLE data is publicly available from the [Space-Track gp_history endpoint](#); daily solar-activity indices are from [CelesTrak’s space-weather file](#).

References

- Giacomo Acciarini, Atılım Güneş Baydin, and Dario Izzo. Closing the gap between SGP4 and high-precision propagation via differentiable programming. *Acta Astronautica*, 226:577–585, 2025. doi: 10.1016/j.actaastro.2024.10.063. arXiv:2402.04830.
- Yoshita Baruah, Souvik Roy, Suvadip Sinha, Erika Palmerio, Sanchita Pal, Denny M. Oliveira, and Dibyendu Nandy. The Loss of Starlink Satellites in February 2022: How Moderate Geomagnetic Storms Can Adversely Affect Assets in Low-Earth Orbit. *Space Weather*, 22(4):e2023SW003716, 2024. doi: 10.1029/2023SW003716.

- Bruce R. Bowman, W. Kent Tobiska, Frank A. Marcos, Cheryl Y. Huang, Chin S. Lin, and William J. Burke. A new empirical thermospheric density model JB2008 using new solar and geomagnetic indices. In *AIAA/AAS Astrodynamics Specialist Conference*, August 2008. doi: 10.2514/6.2008-6438. AIAA 2008-6438.
- J. T. Emmert, D. P. Drob, J. M. Picone, D. E. Siskind, Jr. Jones, M., M. G. Mlynczak, P. F. Bernath, X. Chu, E. Doornbos, B. Funke, L. P. Goncharenko, M. E. Hervig, M. J. Schwartz, P. E. Sheese, F. Vargas, B. P. Williams, and T. Yuan. NRLMSIS 2.0: A whole-atmosphere empirical model of temperature and neutral species densities. *Earth and Space Science*, 8(3):e2020EA001321, 2021. doi: 10.1029/2020EA001321.
- eoPortal. LeoLabs commercial ground-based tracking service for LEO resident space objects. ESA eoPortal Directory; https://www.eoportal.org/ftp/satellite-missions/1/LeoLabs_070122/LeoLabs.html, 2022. Accessed 2026-05-14.
- Felix R. Hoots, Paul W. Schumacher, and Robert A. Glover. History of analytical orbit modeling in the U. S. Space Surveillance System. *Journal of Guidance, Control, and Dynamics*, 27(2):174–185, 2004. doi: 10.2514/1.9161.
- Gunter D. Krebs. Starlink Block v2-Mini. Gunter’s Space Page; https://space.skyrocket.de/doc_sdat/starlink-v2-mini.htm, 2024. Accessed 2026-05-11.
- Anqi Lang and Yu Jiang. Orbit Determination for Continuously Maneuvering Starlink Satellites Based on an Unscented Batch Filtering Method. *Sensors*, 25(13):4079, 2025. doi: 10.3390/s25134079.
- Stijn Lemmens and Holger Krag. Two-Line-Elements-Based Maneuver Detection Methods for Satellites in Low Earth Orbit. *Journal of Guidance, Control, and Dynamics*, 37(3):860–868, 2014. doi: 10.2514/1.61300.
- Jonathan C. McDowell. The Low Earth Orbit Satellite Population and Impacts of the SpaceX Starlink Constellation. *The Astrophysical Journal Letters*, 892(2):L36, 2020. doi: 10.3847/2041-8213/ab8016. GCAT data product at <https://planet4589.org/space/gcat/>.
- Nikolaos K. Pavlis, Simon A. Holmes, Steve C. Kenyon, and John K. Factor. The development and evaluation of the Earth Gravitational Model 2008 (EGM2008). *Journal of Geophysical Research: Solid Earth*, 117(B4):B04406, 2012. doi: 10.1029/2011JB008916.
- Timothy Payne, Felix Hoots, Albert Butkus, Zachary Slatton, and Dinh Nguyen. Improvements to the SGP4 propagator (SGP4-XP). In *Proceedings of the Advanced Maui Optical and Space Surveillance Technologies (AMOS) Conference*, 2022. URL https://amostech.com/TechnicalPapers/2022/AstroDynamics/Payne_2.pdf.
- G rard Petit and Brian Luzum. IERS Conventions (2010). IERS Technical Note 36, International Earth Rotation and Reference Systems Service, Frankfurt am Main, 2010. Verlag des Bundesamts f r Kartographie und Geod sie, ISBN 3-89888-989-6.
- J. M. Picone, A. E. Hedin, D. P. Drob, and A. C. Aikin. NRLMSISE-00 empirical model of the atmosphere: Statistical comparisons and scientific issues. *Journal of Geophysical Research: Space Physics*, 107(A12):1468, 2002. doi: 10.1029/2002JA009430.
- Brandon Rhodes. sgp4: Python implementation of the SGP4/SDP4 satellite-tracking algorithm. Python package; <https://github.com/brandon-rhodes/python-sgp4>, 2024. Implementation of the reference SGP4 code from Vallado et al. [2006]; accessed 2026-05-13.
- Space Exploration Holdings, LLC. Semi-Annual Constellation Status Report, 1 December 2023 to 31 May 2024. Federal Communications Commission filing, IBFS File No. SATMOD2020041700037, 2024. Filed 1 July 2024. Reports an average of 14 thruster firings per satellite over the six-month window for autonomous collision-avoidance maneuvers.
- Space Exploration Holdings, LLC. Reply comments on the Notice of Inquiry, WT Docket No. 25-110: Promoting the Development of Positioning, Navigation, and Timing Technologies and Solutions. Federal Communications Commission filing, 2025.

- David A. Vallado. *Fundamentals of Astrodynamics and Applications*. Space Technology Library. Microcosm Press, Hawthorne, CA, 4th edition, 2013. ISBN 978-1881883180.
- David A. Vallado and Paul J. Cefola. Two-line Element Sets — Practice and Use. In *63rd International Astronautical Congress*, 2012. IAC-12-A6.6.11.
- David A. Vallado and Paul Crawford. SGP4 Orbit Determination. In *AIAA/AAS Astrodynamics Specialist Conference and Exhibit*, August 2008. doi: 10.2514/6.2008-6770. AIAA 2008-6770.
- David A. Vallado, Paul Crawford, Richard Hujsak, and T. S. Kelso. Revisiting Spacetrack Report #3. In *AIAA/AAS Astrodynamics Specialist Conference and Exhibit*, August 2006. doi: 10.2514/6.2006-6753. AIAA 2006-6753.
- J. H. Verner. Explicit Runge–Kutta methods with estimates of the local truncation error. *SIAM Journal on Numerical Analysis*, 15(4):772–790, 1978. doi: 10.1137/0715051.

Sampled Starlink corpus — 501 satellites

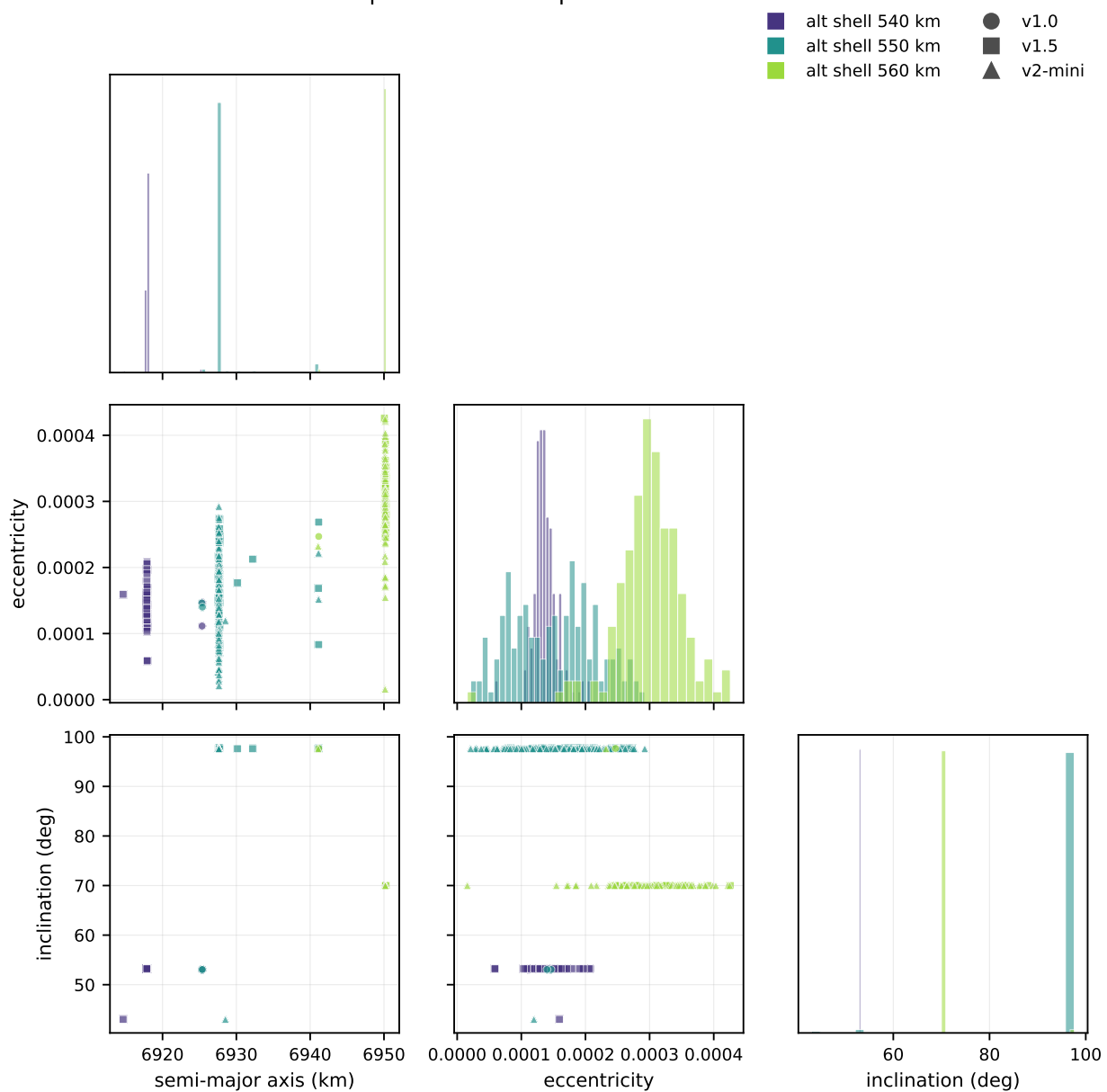


Figure 1: Sampled corpus. Pairwise scatter of semi-major axis, eccentricity, and inclination for the 501 Starlink satellites in the analysis sample. Altitude shell encoded by color, generation encoded by marker shape; diagonal panels show marginal histograms.



SGP4 propagation error vs. time since epoch

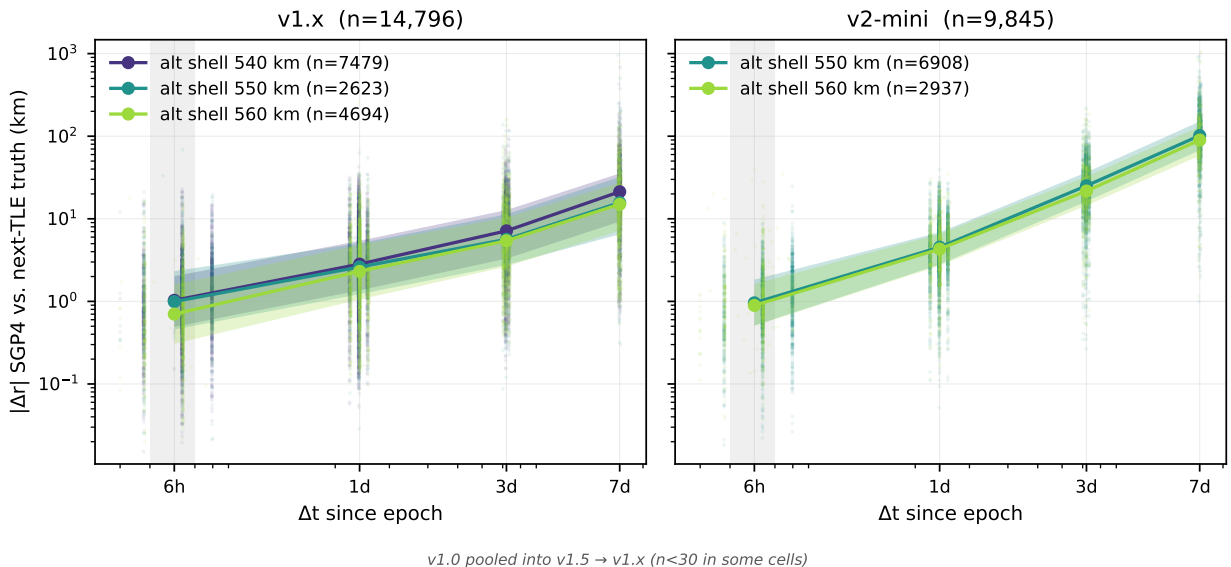


Figure 2: SGP4 propagation error against the next-TLE proxy vs. Δt since epoch, by altitude shell within pooled-generation panels. Light scatter shows individual $(\Delta t, |\Delta \mathbf{r}|)$ pairs; bold markers connected by lines give the per-bucket median and the shaded band gives the 25th–75th percentile range. Log-log axes; identical y -limits to Figure 3. The light grey vertical band marks the consumer-relevant 6 h horizon (the ± 2 h pair-matching tolerance, Section 3.3); this bucket is floor-limited per Section 2.1.



High-fidelity propagation error vs. time since epoch

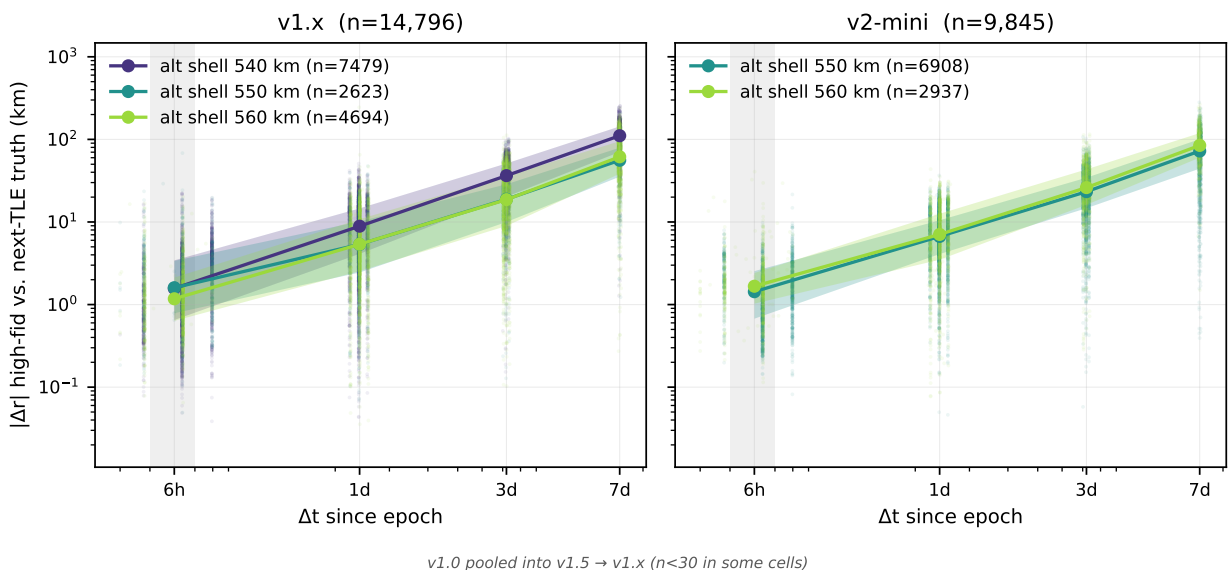


Figure 3: High-fidelity propagation error vs. Δt since epoch, rendered with identical layout and axes to Figure 2 for direct visual comparison. The 6 h consumer-horizon band is shaded as in Figure 2.



Power-law fits: $\|\Delta\mathbf{r}\| \approx A \cdot \Delta t^k$ per altitude shell \times generation

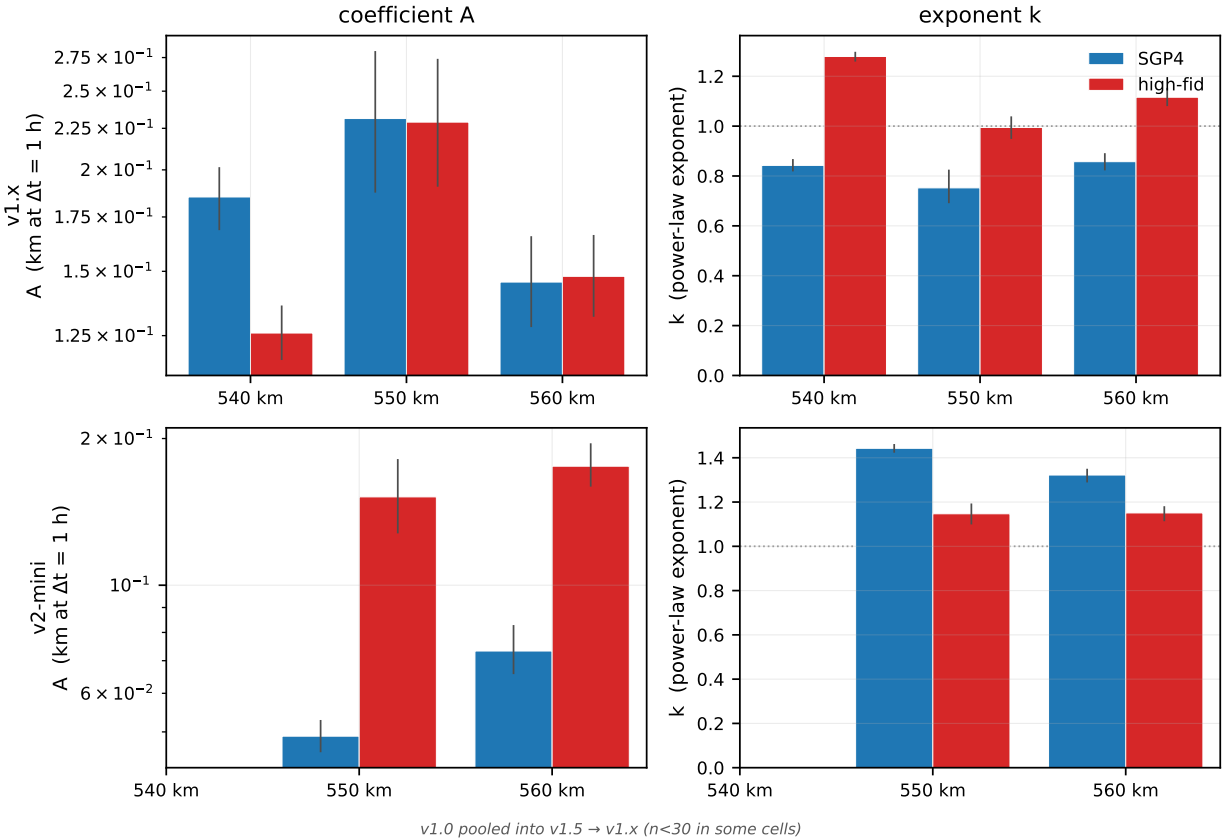
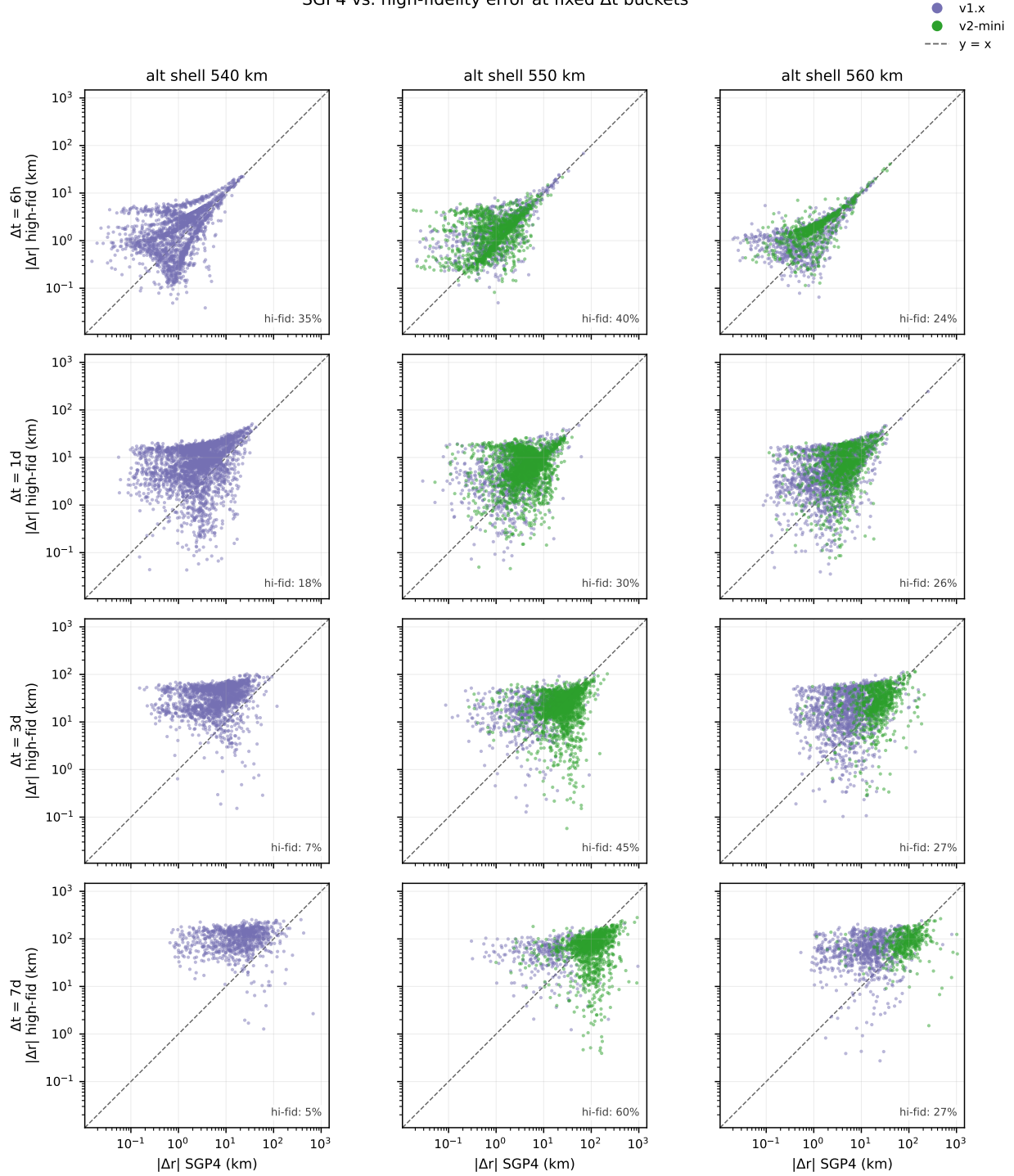


Figure 4: Power-law fits $\|\Delta\mathbf{r}\| \approx A \cdot \Delta t^k$ per (altitude shell \times pooled generation) cell. Bars show the point estimate; vertical lines give 95% bootstrap percentile CIs from 1,000 resamples drawing satellites with replacement and pooling all of each drawn satellite’s pairs in the cell, per the estimator specification in Section 3.8.1. The visual tightness of the CI bars on the well-populated cells reflects the $n \approx 167$ satellites per shell, the geometric narrowness of the Starlink shells in (a, e, i) , and log-axis compression of the per-pair scatter — not under-accounting for within-satellite correlation, which the satellite-level resample is constructed specifically to absorb (Section 3.8.1); the parametric mixed-effects cross-check of Appendix F returns slopes inside the bootstrap CIs on every populated cell. Left subpanel per row: coefficient A on a log axis; right subpanel: exponent k with $k = 1$ marked. Numerical values are listed in Table 5.



SGP4 vs. high-fidelity error at fixed Δt buckets



v1.0 pooled into v1.5 → v1.x (n<30 in some cells)

Figure 5: SGP4 vs. high-fidelity error per pair, at fixed Δt buckets (rows) and altitude shells (columns). Color encodes pooled generation; the dashed $y = x$ line marks parity, so points below are pairs where the high-fidelity model beat SGP4 in 3D L_2 norm. The per-panel label in each lower-right corner reports the fraction of cell pairs below the diagonal (“hi-fid wins”); a bootstrap-quantified per-cell version of the same fraction (plus an along-track-only variant) is in Table 6. A hexbin density variant of the same scatter is in Appendix B (Figure 9).



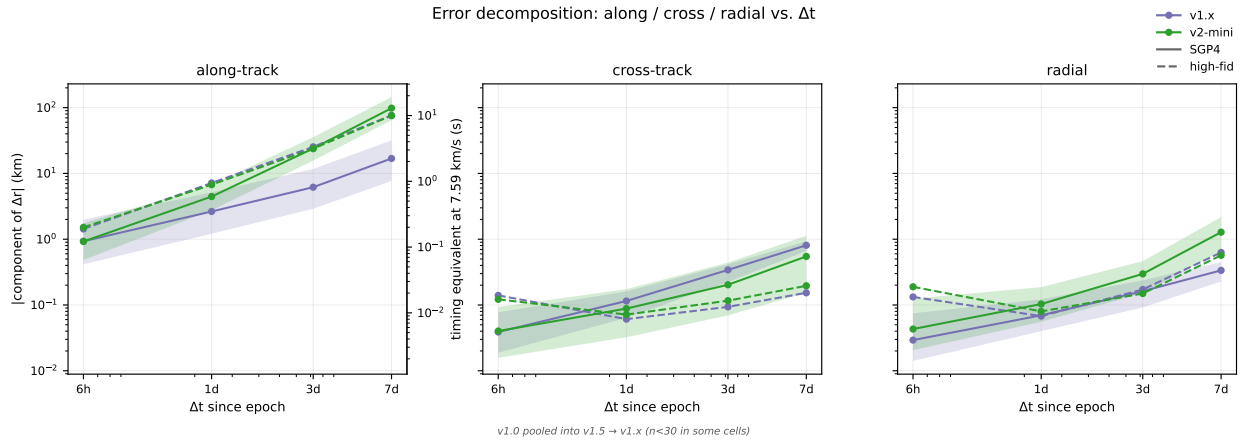


Figure 6: Error decomposition into along-track, cross-track, and radial components of $\Delta \mathbf{r}$ in the next-TLE-proxy RSW frame. Per-bucket medians with IQR ribbons; solid lines are SGP4, dashed lines are high-fidelity; color encodes pooled generation. The along-track panel carries a secondary y -axis in seconds of orbital phase, converted by $\Delta t_{\text{phase}} = \Delta s / v_c$ at the 550 km circular-orbit speed $v_c = \sqrt{\mu / (R_{\oplus} + 550 \text{ km})} \approx 7.59 \text{ km s}^{-1}$, the central-shell value.

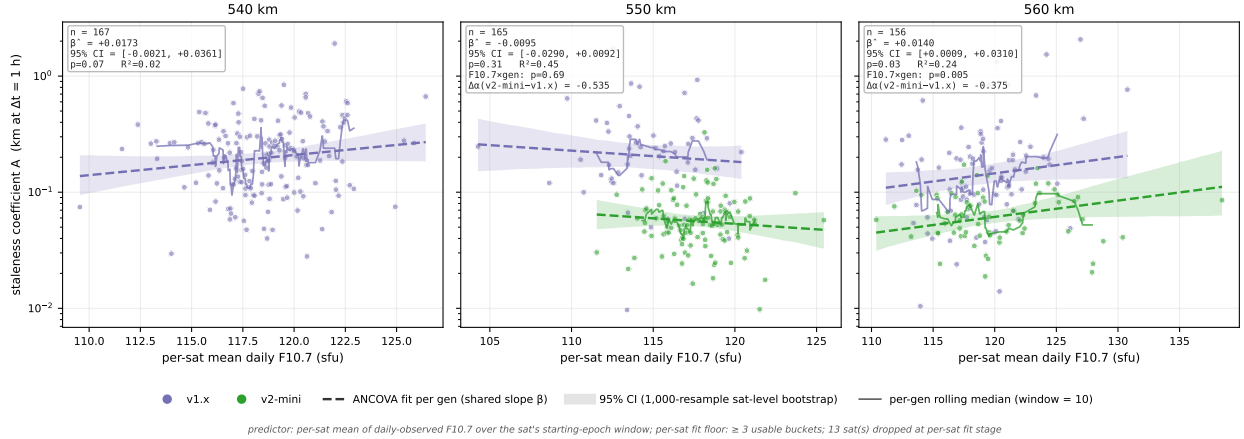


Figure 7: Per-satellite SGP4 staleness coefficient A vs. the mean daily-observed F10.7 flux over the satellite's corpus time window, one panel per altitude shell (540, 550, 560 km). Markers are coloured by pooled generation (purple v1.x, green v2-mini); the 540 km shell has no v2-mini satellites in the corpus (Table 2). Within each panel: per-satellite scatter, a per-generation rolling median (solid) for visual context, and the ANCOVA fit of Eq. (6) drawn as one dashed OLS line per generation present, with 95% percentile CI ribbons. The two lines per panel share the fitted slope $\hat{\beta}$ and differ only in the per-generation intercept $\hat{\alpha}_{\text{gen}}$; ribbons combine the slope and intercept-offset bootstrap distributions consistently. The in-panel annotation reports the satellite count, $\hat{\beta}$, its 95% bootstrap CI, the t -stat p -value for $H_0: \beta = 0$, the model R^2 , the partial- F p -value for the interaction-vs-additive comparison (where the shell carries more than one cohort), and the intercept offset $\hat{\alpha}_{\text{v2-mini}} - \hat{\alpha}_{\text{v1.x}}$.

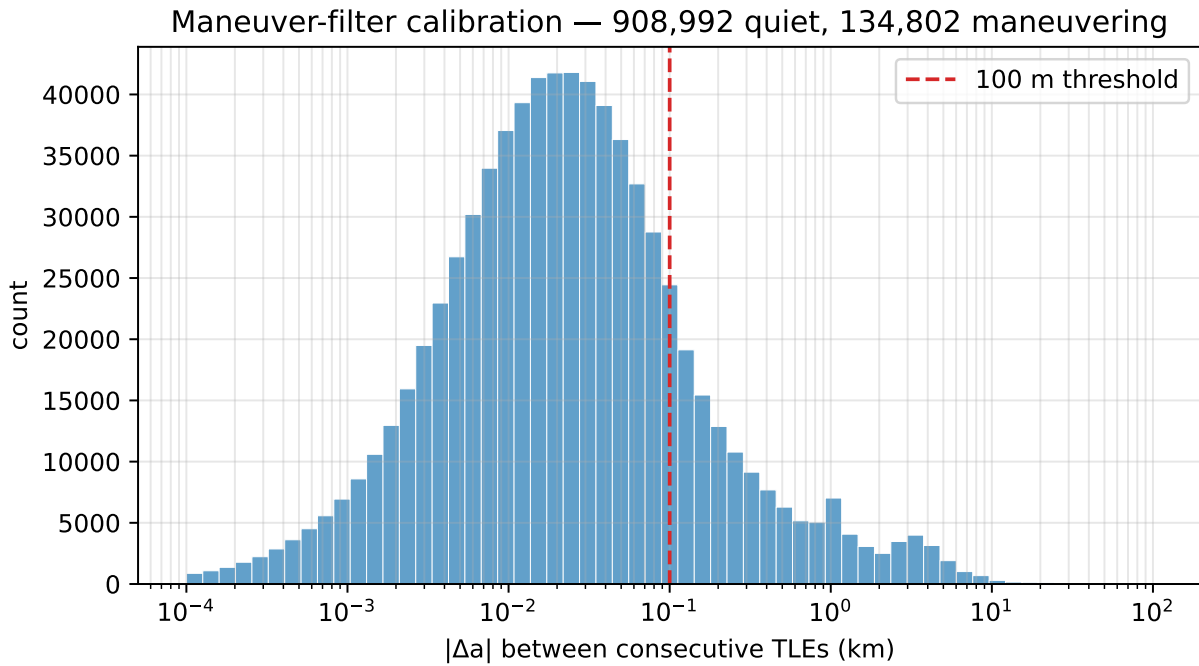
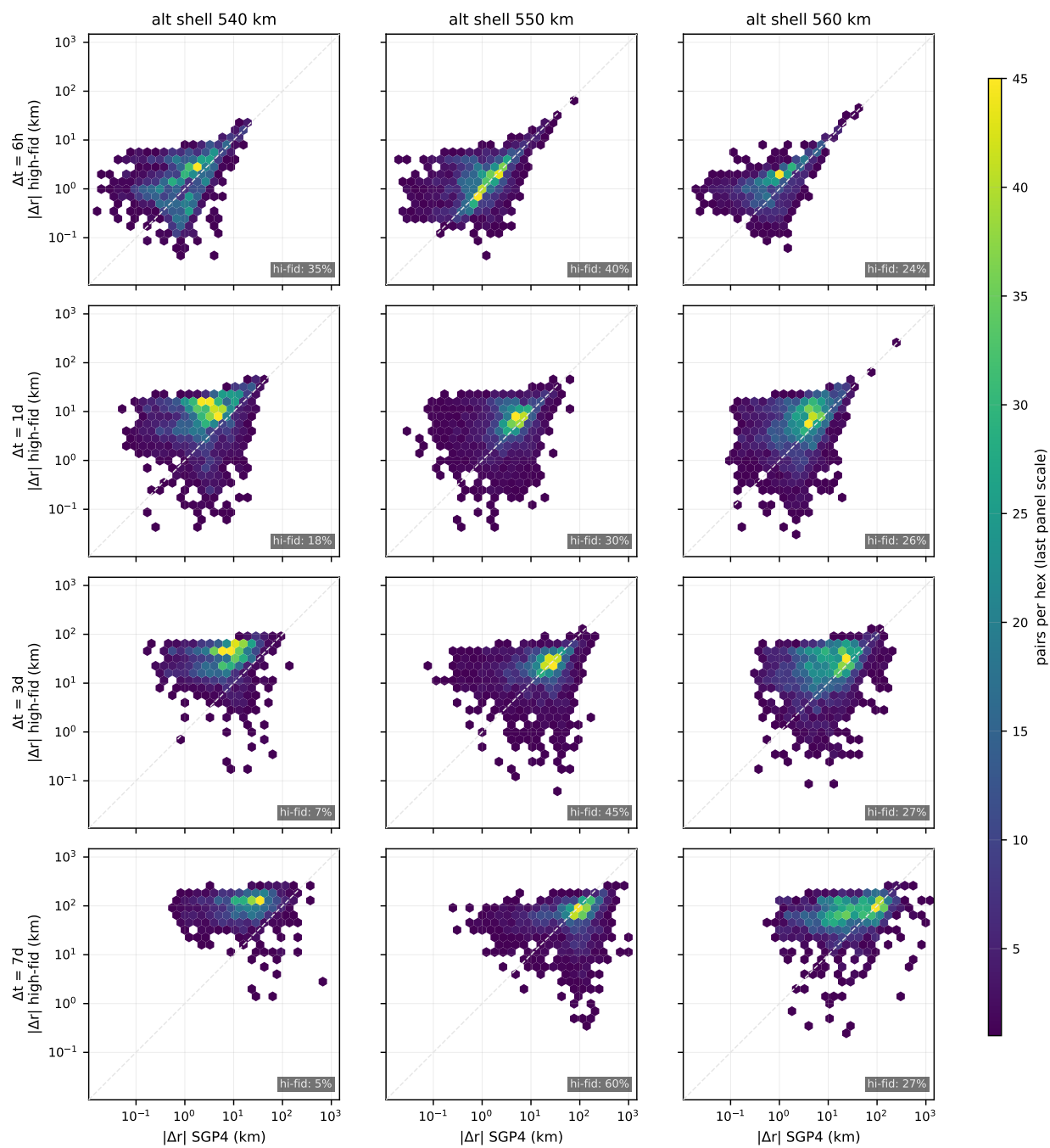


Figure 8: Distribution of $|\Delta a|$ between consecutive Starlink TLEs across the raw cache. The dashed line marks the 100m maneuver filter threshold. The OD-noise mode and the maneuver mode overlap in the 50–200 m region rather than separating at a clean valley (the expected signature of Starlink’s continuous low-thrust station-keeping cadence); the 100 m threshold cuts at the right edge of the OD-noise mode, and the Appendix D sensitivity perturbation tests the choice at ± 50 m.



SGP4 vs. high-fidelity error at fixed Δt buckets (hexbin density)



v1.0 pooled into v1.5 → v1.x (n<30 in some cells)

Figure 9: Hexbin density variant of Figure 5. Each panel is binned in $(\log_{10} |\Delta \mathbf{r}|_{\text{SGP4}}, \log_{10} |\Delta \mathbf{r}|_{\text{hifid}})$ on gridsize = 30 hexes per side, viridis colour ramp with mincnt = 1; per-panel hi-fid-wins fraction inset as in the main scatter.



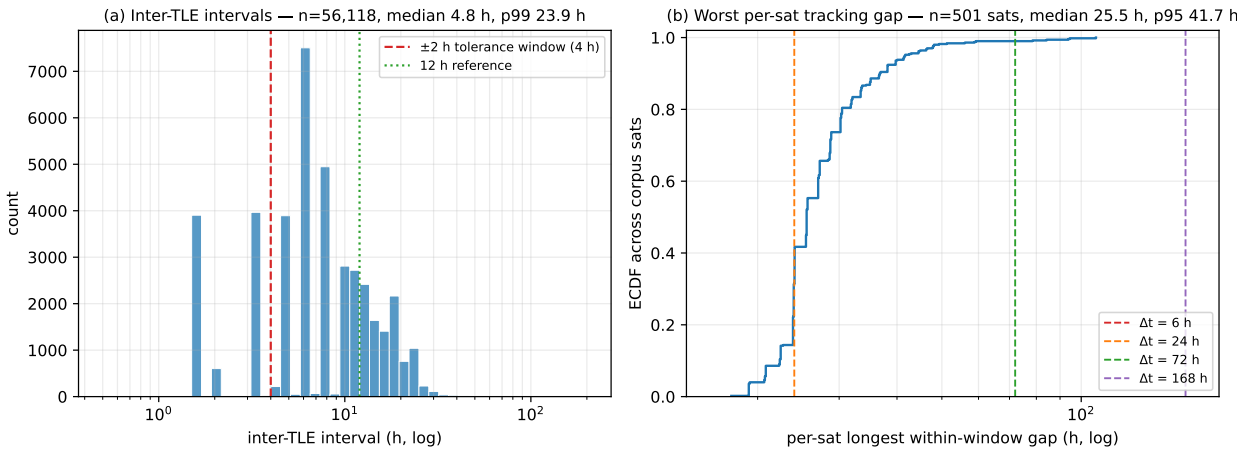


Figure 10: Selection-effect diagnostic for the ± 2 h pair-matching tolerance. (a) Histogram of inter-TLE intervals across the corpus (log-x); the dashed line marks the 4 h-wide tolerance window, the dotted line a 12 h reference. (b) Empirical CDF of per-sat longest within-window gaps across the 501 sampled sats; vertical lines mark the four Δt targets. The 95th-percentile worst per-sat gap (~ 42 h) is well inside the longest Δt target (168 h), so no sat is systematically excluded by the matching tolerance.

